BIRDS

How birds direct impulse to minimize the energetic cost of foraging flight

Diana D. Chin* and David Lentink

Birds frequently hop and fly between tree branches to forage. To determine the mechanical energy trade-offs of their bimodal locomotion, we rewarded four Pacific parrotlets with a seed for flying voluntarily between instrumented perches inside a new aerodynamic force platform. By integrating direct measurements of both leg and wing forces with kinematics in a bimodal long jump and flight model, we discovered that parrotlets direct their leg impulse to minimize the mechanical energy needed to forage over different distances and inclinations. The bimodal locomotion model further shows how even a small lift contribution from a single proto-wingbeat would have significantly lengthened the long jump of foraging arboreal dinosaurs. These avian bimodal locomotion strategies can also help robots traverse cluttered environments more effectively.

INTRODUCTION

Foraging arboreal birds frequently hop or fly between branches by extending long jumps with a few wingbeats. Small birds perform this bimodal locomotion up to 30 times per minute, typically over distances of <1 m and inclinations of <20° (*1*). This visually guided feeding behavior in cluttered habitats not only is critical to the energetics of many extant birds (*2*) but also was likely used by avian precursors, such as *Archaeopteryx* (*3*). The role of bimodal foraging in the evolution of bird flight has yet to be fully resolved. Nevertheless, supporters of both "ground-up" cursorial and "trees-down" arboreal hypotheses agree that the evolution of flight increased foraging gain (*3*–*7*). Excess energy benefits reproduction (*2*), so natural selection of bimodal foraging traits can help explain the proliferation of arboreal foraging birds, including the most diversified modern order, Passeriformes, and the sister group of all landbirds, the hoatzin (*8*). Similar to the behavior proposed for several protobirds (*3*), hoatzin nestlings climb trees with claws, whereas adults perform foraging flights, with flight muscles supported by a reduced sternum (*9*). Understanding the biomechanics of perch-to-perch foraging flights can therefore help mechanistically underpin how protobirds could have honed their foraging flight skills, and fill critical gaps in our understanding of the energetics of extant arboreal birds.

During short foraging flights, birds transfer impulse, the integral of force over time, with their legs to a branch to make a long jump. After toe-off, their wings transfer impulse to the air to support bodyweight. Previous studies quantified bird leg takeoff or landing forces (*10*–*14*), but few examined the transition of weight support between the legs and wings (*15*–*18*). Studies quantifying wing contributions relied on indirect methods to calculate force based on wake flow (*15*, *16*) or body kinematics (*16*–*19*). Further, although foraging flights are motivated by food, most of these biomechanics studies have only recorded escape responses (*10*, *12*, *15*–*17*) or "spontaneous" flights (*11*, *17*). Conclusions from these studies may not apply to foraging; hummingbirds rely less on their legs during takeoffs motivated by escape (*18*), and tits adjust their takeoffs based on a mock predator's velocity (*20*). Although wing forces during foraging flights have been directly measured, these measurements do not include any leg impulses (*21*). The complete transfer of impulse from takeoff to landing has never been measured before for any flying animal, foraging, or escaping.

Department of Mechanical Engineering, Stanford University, Stanford, CA 94305, USA.
*Corresponding author. Email: ddchin@stanford.edu

RESULTS

To determine mechanical energy trade-offs made during arboreal foraging, we studied how Pacific parrotlets (*Forpus coelestis*), arboreal Psittacidae, transferred impulse during voluntary, perch-to-perch flights to get a seed. We measured leg-generated forces with instrumented perches and wing-generated vertical forces using a new aerodynamic force platform (AFP) (Fig. 1A and fig. S1) (*21*). The birds hopped or flew level over distances of 20, 40, and 75 cm while also ascending (+20°) and descending (−20°) over 75-cm distances (Fig. 1B; see Materials and Methods for further details). Our time-resolved in vivo force recordings recovered the complete transfer of vertical impulse between the legs and wings (Fig. 1C). The birds fully supported their bodyweight (~100%; Fig. 1D), as predicted for bimodal locomotion starting and ending at rest (see the Supplementary Materials).

Leg and wing impulses during different foraging flight variations

During 20-cm flights, parrotlets mostly use partial wingbeats, or none (Fig. 2A and fig. S2A). The partial downstrokes average 70% bodyweight impulse, roughly half that of full downstrokes at similar velocities (see Materials and Methods, fig. S2B), whereas upstrokes are inactive. During longer flights, upstroke contributions increase before landing (Fig. 2, B to E). At 75 cm, parrotlets consistently fold in their wings mid-flight to bound, generating almost no weight support (Fig. 2, C to E).

Although wing contributions increase with distance, the legs generate the majority of total bodyweight support across all foraging flight variations (Fig. 1D). During takeoff (Fig. 3A), parrotlets use their legs to accelerate to ~80 to 100% of average flight speeds. Horizontal leg impulse (fig. S3) is also significant for decelerating during landing (Fig. 3B). As parrotlets visually estimate the time to contact, they only brake sufficiently with their wings for a "controlled collision" (see Tau function in Materials and Methods). Prominent leg use may be preferred, because it is more efficient to locomote by pushing against solid substrates with the legs than by pushing against air with the wings (*15*, *22*).

The parrotlets further improve efficiency during ascending flights by making controlled collisions with the landing perch from below (Fig. 3B) such that the net vertical impulse is near zero (Fig. 3C). As inclination decreases from +20° to −20°, vertical impulse increases for landing (Fig. 3, B and C) and decreases for takeoff (Fig. 3, A and C). Parrotlets markedly direct these leg takeoff impulses consistently,

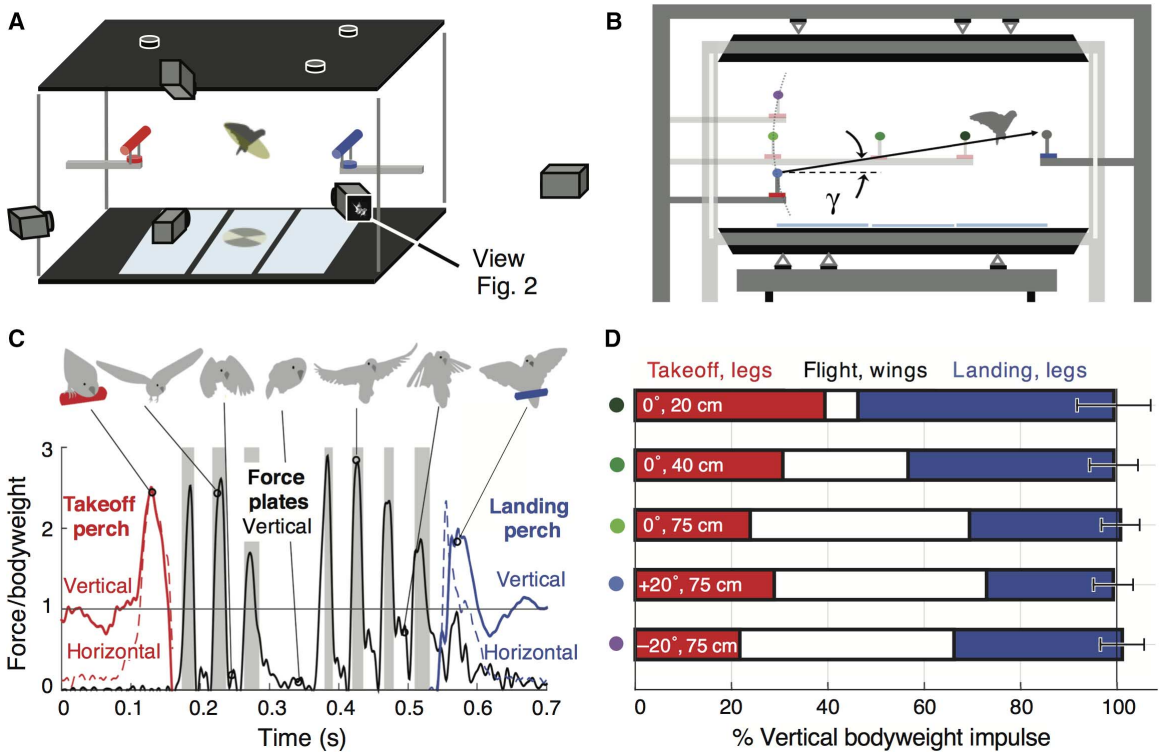

Fig. 1. A new aerodynamic force platform accurately measures the complete transfer of vertical impulse generated during foraging flights. (**A**) Two plates, each connected to three force sensors (black discs), integrate the pressure field along the top and bottom surfaces of the "control volume" in which the bird flies. Instrumented perches measure leg forces during takeoff (red) and landing (blue). Five kinematic high-speed cameras are synchronized with force measurements at 1000 Hz. Mirrors on the bottom plate provide a ventral view of the projected area swept out by the wings (see Materials and Methods). (**B**) To test how distance and inclination (γ) between perches modify bimodal locomotion, five variations were used: 20-cm (dark green), 40-cm (green), and 75-cm (light green) level (γ = 0°) versus 75-cm ascending (γ = +20°; light blue) and descending (γ = −20°; purple) flights. (**C**) A typical 75-cm, level flight force recording shows parrotlets support bodyweight primarily with their legs (red and blue) and wing downstrokes (black line and gray shaded regions). (**D**) Legs are the dominant weight support contributors. Bars show mean ± SD for $N = 4$ birds and $n = 5$ flights each, except that 20- and 40-cm wing contributions are $n = 10$ (see Materials and Methods). The platform and perches recover ~100% of vertical impulse needed to support bodyweight.

especially considering the erratic takeoff angles exhibited by birds in previous biomechanics studies (*10*, *11*, *23*). This discrepancy may be explained by motivation; whereas the birds in these previous takeoff studies flew to escape, the foraging parrotlets in our study flew voluntarily. We expect that these voluntary behaviors are more energetically efficient than escape responses, but currently there are no existing models that combine a long jump with flapping flight to assess the energetic benefit of directing leg impulse.

A bimodal locomotion model relating takeoff angle with mechanical energy requirements

We thus developed a bimodal foraging flight model to evaluate how takeoff angle θ affects the mechanical energy E that the legs and wings need ($E = E_{legs} + E_{wings}$; see Materials and Methods for details) to cover the distance. The long jump energy E_{legs} is based on measured leg-extension and toe-off velocities and is calculated using an established human long jump model (*24*). The aerodynamic energy, E_{wings}, includes the profile, induced, and climbing power required to support bodyweight, as well as the power needed to accelerate beyond toe-off and decelerate before touchdown. These calculations build upon quasi-steady flapping flight models used throughout the animal flight literature, which show that reasonable mechanical energy estimates can be made based on wing and body kinematics (*25*–*33*). We extend these kinematics-driven flight models by integrating our direct force measurements. Further, to relate leg impulses during takeoff with wing impulses during flight, we combine them in a long jump/flight model. This new bimodal locomotion model shows how more wing energy is needed to obtain climb velocity at small takeoff angles, θ, and forward velocity at large θ. Large θ are also costly, because more leg muscle force is used to counteract bodyweight (*24*).

Our induced power estimates included the increase in upstroke weight support from takeoff wingbeats (Fig. 3D) to landing wingbeats (Fig. 3E). Parrotlets increase the ratio of upstroke to downstroke vertical impulse with body angle irrespective of flight inclination (Fig. 3F and fig. S4A). Elevated body angle might thus explain the active upstroke observed in turning pigeons (*19*). We also found that actuator disc area, the horizontally projected area swept out by the wings, increases with body angle (fig. S4B). Larger impulse ratios and actuator disc areas both reduce induced power, so we also included these effects into the model (see Materials and Methods).

Our bimodal locomotion model predicts energy-minimizing takeoff angles, θ, between 0.1 and 1.3 SDs (table S2) of the mean θ that parrotlets use for each flight variation (Fig. 4A). Optimal θ varies substantially with inclination, which suggests that parrotlets must estimate inclination to select efficient θ. If the average θ chosen for ascending flight is used for descending, then E would increase by ~23%.

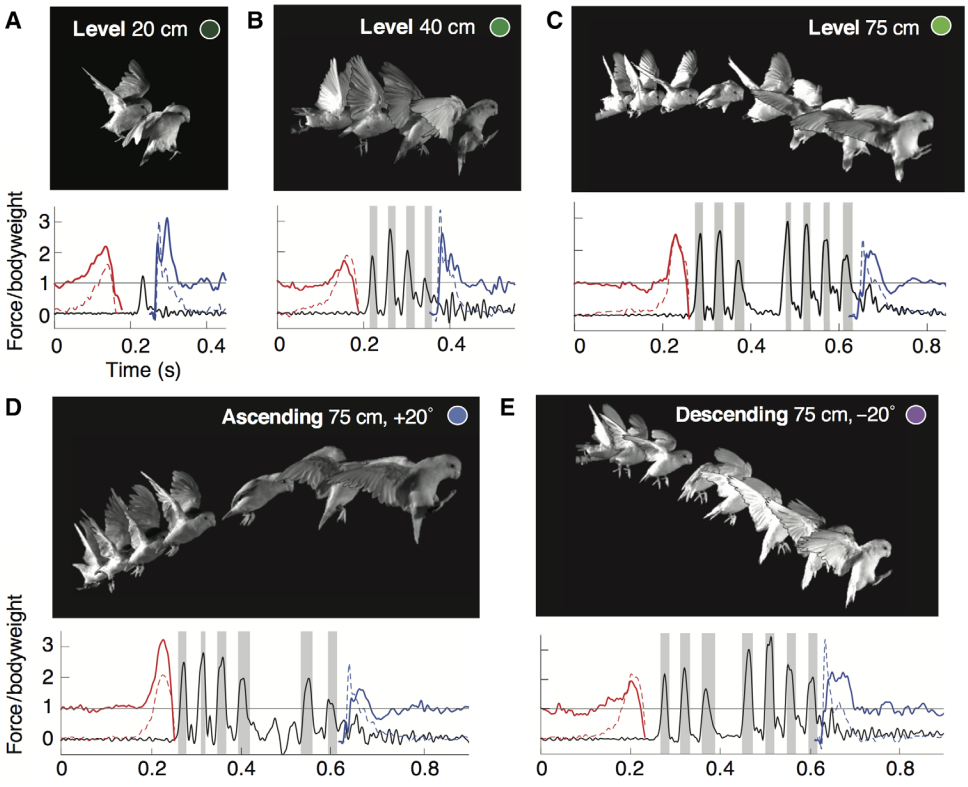

Fig. 2. Parrotlets primarily support bodyweight during downstrokes, but as they pitch up before landing, upstroke contributions increase. Parrotlets frequently fold their wings to bound mid–75-cm flights, which contributes little to weight support. Solid lines indicate the vertical forces on the takeoff perch (red), force plates (black), and landing perch (blue) (see legends in Fig. 1C). (**A**) Parrotlets primarily long jump up to 20 cm, beyond which they flap their wings to support their bodyweight. (**B** and **C**) Level long jump and flight over 40 and 75 cm. (**D** and **E**) During the 75-cm ascending and descending flights, parrotlets adjust the force they exert on the takeoff versus landing perch. Frames (from movies S1 to S5) showing the bird at the start of each downstroke are overlaid in corresponding photos. An additional frame showing the bird bounding is included in (C) to (E). All frames shown were recorded by the camera indicated in Fig. 1A, so the perspective may give the impression of nonlevel flight in (A) to (C). Colored circles encode flight variations for Figs. 3 and 4.

Mechanistic insight into the evolution of foraging flight

The limited weight support generated by parrotlet downstrokes during 20-cm flights, when averaged over an entire wingbeat, is similar to the ~15 to 30% bodyweight support that incipient chukar wings generate during symmetric flapping (*34*). A single proto-wingbeat by *Archaeopteryx* and other small bird antecedents such as *Microraptor* may have also generated ~25 to 30% bodyweight support, with stroke amplitude restricted to 70° (*35*). On the other hand, large bird antecedents further removed from modern birds, such as *Protarchaeopteryx* and *Caudipteryx*, probably generated much less weight support with their wings (*35*). We thus modified our model to test the potential benefit of flapping protowings for parrotlets and these bird antecedents. Whereas previous proto-flier models assume that takeoff speed is augmented by running (*5*) or flapping (*35*), or that flapping is preceded by gliding (*6*, *7*), we assumed, informed by parrotlet foraging behavior, that flapping commences after toe-off, with takeoff angles optimized for range (see Materials and Methods for details). For short long jumps assisted by a single proto-wingbeat, we found that delaying the onset of flapping reduces the extension of the long jump range (fig. S5A). To compare the maximum possible horizontal range of a wing-assisted jump with that of a nonassisted jump for parrotlets and bird antecedents, we assumed that the proto-wingbeat started immediately after toe-off. This is likely an overestimate of actual performance, because we found that parrotlets began their partial wingbeats between zero and two wingbeat periods after toe-off during the short 20-cm flights. Whereas parrotlets optimize takeoff angle, we did not find evidence that they time their wingbeat impulse to minimize power (fig. S5, B and C). Instead, we hypothesize that they use wingbeat timing for flight control, exemplified by behaviors such as wingbeat pauses (Fig. 2, C to E), and the visually guided controlled collisions for landing (see Tau function in Materials and Methods).

Our bimodal locomotion model shows how protowings could significantly extend long jumps and thus increase foraging range, particularly for smaller proto-fliers (Fig. 4B). For example, adding a single downstroke generating only 30% bodyweight support (dashed line in Fig. 4B) would increase *Archaeopteryx* and *Microraptor* long jump ranges by ~20%—by investing more energy into locomotion, these proto-fliers could have expanded their foraging volumes in trees and gained critical advantages over competitors. The predicted nearly linear relationship between the long jump range and proto-wingbeat weight support arises from the direct relation between the long jump range and the time spent in the air. This air time increases almost linearly with the vertical impulse imparted by the partial downstroke. To fully understand this result, we linearized the bimodal model (see Materials and Methods) and show that the percent increase in the long jump range

$$\Delta X \approx \frac{F_{DS} t_{DS}}{m v_{TO,z}} * 100 \quad (1)$$

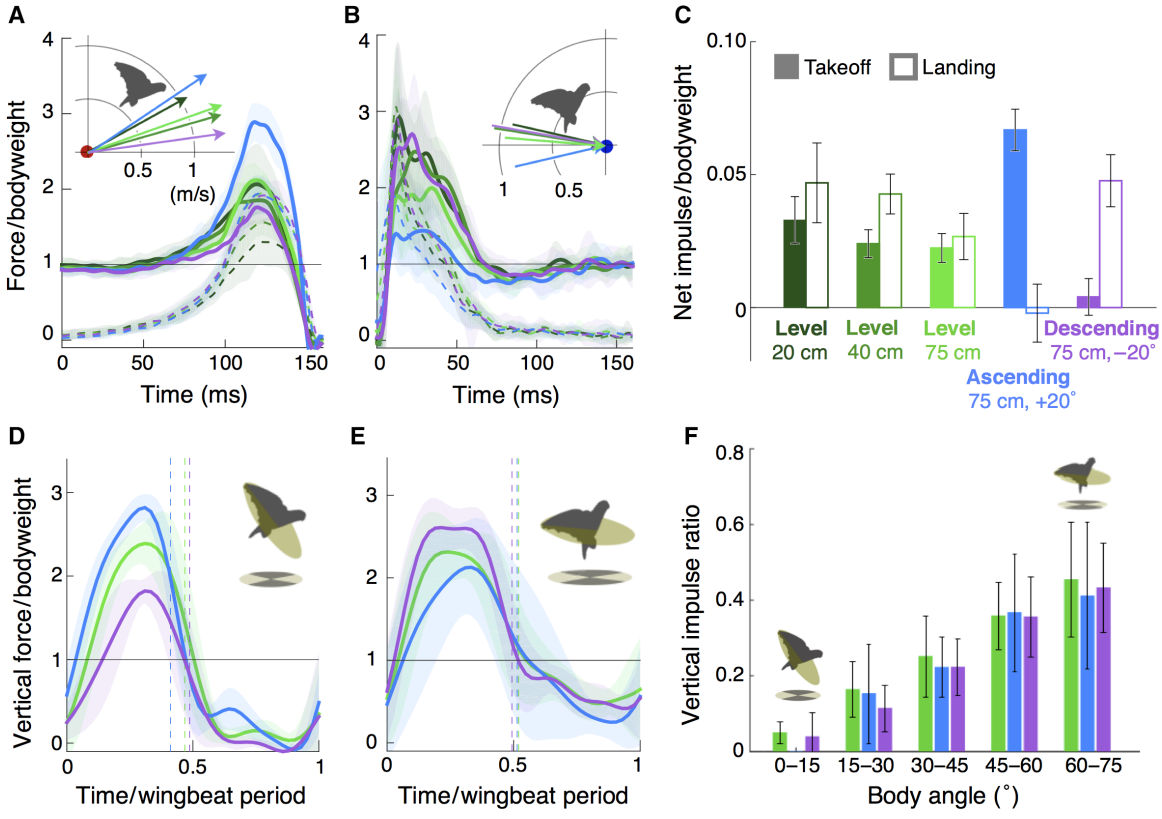

Fig. 3. As inclination increases from −20° to 20°, parrotlets increase takeoff impulse and decrease landing impulse. Across all inclinations, upstroke contributions increase with body angle. During takeoff (**A**) and landing (**B**), the legs exert vertical (solid line) and horizontal forces (dashed line) on the perch to accelerate and decelerate. Takeoff angle increases with inclination, whereas landing angle decreases. In contrast, takeoff speed remains relatively constant across 40- and 75-cm flights (inset; table S1). (**C**) Net impulse is the integrated vertical leg force [(A) and (B)] minus bodyweight. Impulse transfer shifts from landing to takeoff for ascending flight, and vice versa for descending. (**D**) During the first wingbeats after toe-off (see Materials and Methods for wingbeat selection criteria), bodyweight is primarily supported by downstroke impulse (dashed boundaries, end of downstroke). (**E**) Just before touchdown, the upstroke contribution to bodyweight support increases. Bird avatars show how body angle and actuator disc area increase from takeoff to landing wingbeats. (**F**) The upstroke to downstroke vertical impulse ratio increases with body angle, regardless of flight inclination. (A to C) Panels show mean results for each flight variation with $N = 4$, $n = 5$. (D to F) Panels show mean results for 75-cm variations with $N = 4$, $n = 3$. SDs are shown by shaded regions in (A), (B), (D), and (E) and by error bars in (C) and (F).

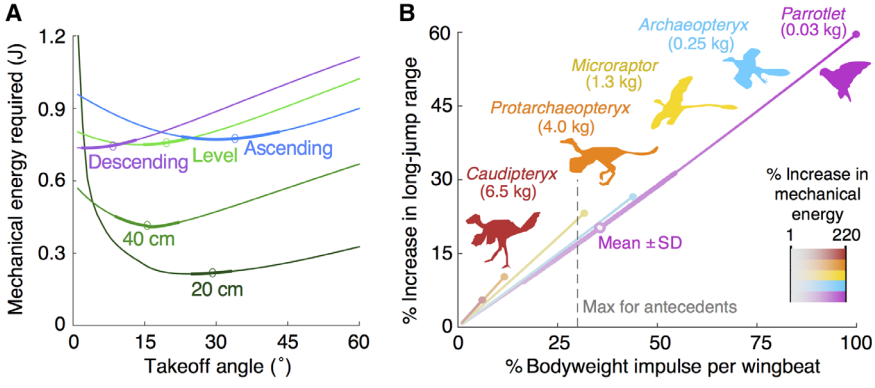

Fig. 4. Foraging parrotlets select takeoff angles that minimize the mechanical energy needed to extend long jumps with flapping wings. The long jumps of parrotlets and their antecedents are greatly extended by (proto)wingbeats. (**A**) The mechanical energy required to long jump and fly between perches depends on takeoff angle, distance, and inclination. Circles mark actual average takeoff angles used, and bolded regions denote SDs, showing that parrotlets preferred close to optimal long jumps. (**B**) Even one proto-wingbeat, with modest aerodynamic weight support during the downstroke and an inactive upstroke, extends the long jump range of all birds and their antecedents substantially [bird antecedent masses; (*35*)]. The increase in energetic cost required is offset by foraging gain. More powerful wingbeats require a smaller body mass, consistent with evolutionary trends in bird antecedents (*37*). Simulated proto-wingbeats were limited to those that would require a muscle mass–specific power within what parrotlets require for a downstroke with full weight support (see Materials and Methods for details). The vertical dashed line indicates 30% bodyweight support, which smaller bird antecedents were likely capable of generating with their protowings (*35*). The open circle (mean) and bolded region (±SD) on the parrotlet curve show the predicted increase in the long jump range based on the measured exerted impulse during 20-cm flights ($N = 4$, $n = 5$; except for two flights, where the bird did not flap its wings).

is proportional to the vertical force generated during the downstroke F_{DS} and the duration of the downstroke t_{DS} and inversely proportional to body mass m and the vertical component of the takeoff velocity $v_{TO,z}$. We can also express this equation in terms of the percent bodyweight impulse per wingbeat J_{WB}, which we plot on the horizontal axis in Fig. 4B

$$\Delta X \approx \frac{2gt_{DS}}{v_{TO,z}} J_{WB} \quad (2)$$

This linearization closely predicts the simulated results (fig. S6), with a maximum percent error of 14% across all antecedents.

DISCUSSION

From Eq. 1, we see that the long jump range increases as the vertical impulse generated by the proto-wingbeat increases, and decreases as the leg impulse is oriented more vertically instead of horizontally. In addition, from Eq. 2 and Fig. 4B, we see that larger protobirds with slower wingbeats experience greater returns in the long jump range. However, aerodynamic power requirements increase much more rapidly with body mass than wingbeat duration (*36*). As a result, large bird antecedents such as *Protarchaeopteryx* and *Caudipteryx* probably could not generate significant weight support with their partial wingbeats, but they could still benefit from incremental increases in their long jump range. As our model shows, these advantages would have grown as successive bird antecedents became smaller and increased their wing-loading capabilities (Fig. 4B), which is consistent with the sustained miniaturization exhibited along the evolutionary path from theropods to modern birds (*37*). Regardless of how flapping flight evolved, extending long jumps with proto-wingbeats to increase foraging gain provides a self-reinforcing, gradual path through which protobirds could have honed their flight skills.

By directing jumps and flapping their wings, extant and ancestral birds can thus increase foraging effectiveness in arboreal habitats and allocate more energy toward reproduction and survival. Similarly, bimodal robots with legs and active wings would benefit from optimizing takeoff angles to locomote more efficiently in cluttered environments.

MATERIALS AND METHODS

Experimental design

The objective of this study was to quantify how birds generate the aerodynamic weight support needed to fly from perch to perch when foraging in trees. To do so, we measured the aerodynamic forces and kinematics of Pacific parrotlets flying across distances and inclinations characteristic of foraging flight (*1*). Pilot studies demonstrated that parrotlets tended to jump short distances, flap continuously for intermediate distances, and use flap-bounding flight for longer distances; the three tested distances (20, 40, and 75 cm) were selected to cover this range of behaviors. To study ascending and descending flights, the takeoff perch was moved down or up so that the inclination between perches was ±20°. After each flight, all force sensors and kinematic cameras were posttriggered (Quantum Composers, model 9618+) to synchronize all measurements.

Birds and training

We trained four Pacific parrotlets (*F. coelestis*; 27.8 ± 0.1 g, two male and two female, 20-Hz wingbeat frequency) to fly between the two perches in the AFP (fig. S1). Parrotlets are arboreal, ecological generalists (*38*), so the findings of this study are expected to be applicable to many other arboreal birds. Each parrotlet was trained using habituation and positive reinforcement, wherein the bird was rewarded with millet seeds when it flew to the perch that the trainer pointed at using a finger or a target stick. All birds were also trained to step voluntarily into custom-built carry boxes for transfer between their housing and the experimental setup (food and water provided ad libitum; cages had enrichment, animals were not sacrificed, and all training and experimental procedures were approved by Stanford's Administrative Panel on Laboratory Animal Care). Perch familiarity has been shown to affect landing kinematics and forces in pigeons (*13*), so to avoid confounding effects, multiple perch-to-perch flights were made by each parrotlet before any experimental data were recorded.

Aerodynamic force platform

To directly measure wing forces, the takeoff and landing perches were set inside the flight chamber (0.905 m × 1.004 m × 0.604 m) of a newly developed AFP, the working principles of which have been described in detail by Lentink *et al.* (*21*) for a much smaller AFP. The AFP used in this experiment (fig. S1A) was made up of three separate structures to avoid mechanical coupling: the inner flight chamber, the top plate and the truss structure that it hung from (the external frame) (fig. S1B), and the bottom force plate and its supporting structure (fig. S1C). Each force plate consisted of a light and stiff carbon fiber plate (1 m × 0.6 m) connected in a statically determined manner to three Nano43 sensors (six-axis, SI-9-9.125 calibration; ATI Industrial Automation) sampling at 1000 Hz with a resolution of 2 mN. The sensors were attached directly to stiff support structures that rest statically determined on the ground. The force plates integrated the pressure field along the top and bottom surfaces of the closed "aerodynamic control volume" in which the bird flew; the vertical force generated by the wings was therefore determined by summing forces measured by both force plates (*21*). The side walls of the flight chamber were made up of acrylic sheets to enable visual access for kinematics. A small hole was cut into one side wall for the landing perch to connect to the outer frame, and a narrow slot was cut into the opposite side wall so the takeoff perch could connect to the outer frame and be moved up and down to test ascending and descending flights. A sliding door on a third wall of the AFP's inner flight chamber enabled us to move birds in and out of the AFP and to cue them for each flight. Force error due to omitting shear stress on the side walls was empirically determined [using methods described by Lentink *et al.* (*21*)] to be less than 4% of total force. As with wind tunnel studies, wall effects were present in the AFP but cause similarly low levels of flow field interference because of the large flight chamber volume. We also verified, using quadcopter studies, that vortex wakes hitting the platform did not affect the accuracy of aerodynamic force measurements (*21*).

Instrumented perches

To measure leg forces, the takeoff and landing perches inside the AFP (fig. S1D) were each instrumented with an ATI Nano43 sensor (1000-Hz sample rate and 2-mN resolution). The perches themselves were constructed from 18-cm sections of $^5/_8$-inch-diameter (1.59 cm) wooden dowels that the parrotlets were accustomed to perching on inside their usual flight cages. Although the tree branches that birds forage on in nature may often be more flexible than these dowels, Bonser *et al.* (*12*) did not find any significant differences in perches of different flexibilities, and the stiffness of our perches enabled us to maintain high natural frequencies

for cleaner force measurements. Extending the takeoff perch for the 20- and 40-cm flights would have significantly lowered the natural frequencies of the system if it remained attached to the external frame. As a result, the perch was instead fixed to a separate structure that stood outside of the AFP and extended into the setup through the sliding window. Forces from the instrumented perch when it was fixed to this stand were not included in our analyses; to get measurements of takeoff and landing forces for five flights per bird, we recorded five flights with the bird taking off from the original landing perch and five flights with the bird flying toward the landing perch (wingbeat forces were thus averaged over 10 flights per bird for the 20- and 40-cm variations in Fig. 1D, whereas leg forces were averaged over five takeoffs and five landings). For kinematic analysis, we averaged over the five flights in which the bird was flying toward the original landing perch.

Force data processing

All force measurements were filtered using an eight-order Butterworth filter with a cutoff frequency of 100 Hz, approximately five times the flapping frequency of the parrotlets. With both instrumented perches attached to the outer frame of the AFP, all natural frequencies of the setup were above 100 Hz (minimum peak frequency of 138 Hz for the top plate, 102 Hz for the bottom plate, 168 Hz for the takeoff perch, and 106 Hz for the landing perch, determined by measuring the frequency response of each structure after imparting an impulse with a carbon fiber rod). This enabled us to filter out noise inherent to the system without affecting the integrity of the relevant data.

Kinematics

Five high-speed cameras (four Phantom Miro M310s and one LC310, 1280 × 800 resolution), synchronized with each other and all force sensors, were positioned around the setup, as shown in Fig. 1A, to determine the start and end of each wingbeat and capture other kinematics of each flight. For a ventral view, one camera was directed at a panel of three mirrors set on the bottom plate at an angle of 11° (the mirrors did not affect the natural frequencies of the bottom plate). The 20- and 40-cm flights were filmed at 1000 Hz, and the 75-cm flights were filmed at 3000 Hz. Cameras were calibrated using the DLT software (*39*) with an average DLT error of less than 2%. The position of the bird's eye and the tip of its tail were manually tracked in each frame, and the tracked data were then digitally filtered (eight-order Butterworth, 100-Hz cutoff frequency). Using the assumption that the bird's head and eye do not move significantly relative to its center of mass, the eye position was differentiated to determine the velocity of the bird. Takeoff and landing angles and speeds (table S1) were determined from the horizontal and vertical velocity components at the end of takeoff and the start of landing (defined in the following section). Body angle was estimated as the angle from the horizontal to a line connecting the eye to the tip of the tail. Using the ventral view of each flight, the amplitude of the projected stroke angle for estimating actuator disc area was determined by averaging the angles swept out by the right and left wings (estimated by the angle between lines connecting the shoulder to the wingtip at its most anterior and most posterior positions during each wingbeat).

Takeoff and landing impulse

Takeoff impulse was calculated by integrating takeoff perch forces from the start of push-off to the end of toe-off. Toe-off times were identified from our synchronized high-speed video. To integrate over a consistent time period for all trials, push-off was defined to start 150 ms before toe-off, which corresponded to when measured horizontal and vertical perch forces began to change. Landing impulse was similarly determined; landing perch forces were integrated starting from touchdown (identified from the high-speed video) and ending after 200 ms, which corresponded to when the horizontal force had decayed and when the vertical force had returned to the bodyweight of the bird. The net vertical impulse (Fig. 3C) was calculated by integrating the vertical force traces and subtracting out the bodyweight impulse imparted by gravity over the same time period. Horizontal takeoff and landing impulses are shown in fig. S3.

Tau function

Because foraging is a visually guided behavior, we quantified braking effort with a parameter used in previous studies of visual control during bird landings (*40*, *41*). The tau function $\tau(t)$ is a first-order approximation for the time to contact, defined as the distance to the destination ($-x$) divided by the speed of approach (*41*). If the time rate of change of this function ($\dot{\tau}$) is held constant between 0 and 0.5, then braking decreases until the bird stops at the landing perch. If $\dot{\tau} = 0.5$, then braking is held constant and the bird stops again at the landing perch. When $0.5 < \dot{\tau} < 1$, braking increases, and the bird makes a controlled collision with the landing perch. Values greater than 1 indicate a collision with the landing perch (*41*). For each flight, x was calculated at each point in time as the distance between the current position of the eye and the position of the eye when the feet first make contact with the perch. The speed of approach was determined by taking the time derivative of x. A linear regression for the values of τ over the last 200 ms before landing was then performed for each flight (three flights per bird per variation). All R^2 values corresponding to the linear regressions for 40- and 75-cm flights were at least 0.96, indicating that the birds maintained a fairly constant value for $\dot{\tau}$, which was given by the slope of each regression line. The resulting $\dot{\tau}$ values for flights from each flight variation were then averaged (table S3). All values fell between 0.5 to 1, the range that corresponds to a controlled collision with the landing perch (*40*, *41*). That is, rather than expending greater energy to brake sufficiently for stopping precisely at the perch, the parrotlets braked with their wings just enough for a controlled collision, relying on their legs to come to a complete stop.

Expected total vertical impulse

Because all perch-to-perch flights start and end at rest, we expect the total vertical impulse imparted by the legs and wings to equal full bodyweight support. That is, the weight support WS (vertical force) generated by a bird of mass m, when averaged over the time t of each flight, should be equal to its bodyweight mg. We show this mathematically using conservation of momentum in the vertical (z) direction (see below). We denote the vertical component of force as F_z, the vertical component of velocity as v_z, takeoff time as t_{TO}, landing time as t_{LD}, and the total flight time as ΔT

$$\begin{aligned} \sum F_z &= \frac{d}{dt} m v_z = \mathrm{WS}(t) - mg \\ m dv_z &= \Big(\mathrm{WS}(t) - mg\Big) dt \\ m\int_{t_{TO}}^{t_{LD}} dv_z &= \int_{t_{TO}}^{t_{LD}} \mathrm{WS}(t) dt - mg\int_{t_{TO}}^{t_{LD}} dt \\ m\Big(v_z(t_{LD}) - v_z\,(t_{TO})\Big) &= \int_{t_{TO}}^{t_{LD}} \mathrm{WS}(t) dt - mg\Delta T \\ 0 &= \int_{t_{TO}}^{t_{LD}} \mathrm{WS}(t) dt - mg\Delta T \end{aligned} \tag{3}$$

The first term on the right-hand side of Eq. 3 is the total vertical impulse generated by the legs and wings of the bird, and the second term is equal to the impulse due to gravity. We thus expect the combined vertical leg and wing impulses to sum to the bodyweight impulse, as in Fig. 1D. Alternatively, we can also express Eq. 3 in terms of the time-averaged weight support $\overline{\mathrm{WS}}$ by dividing by ΔT

$$\overline{\mathrm{WS}} = \frac{1}{\Delta T}\int_{t_{\mathrm{TO}}}^{t_{\mathrm{LD}}} \mathrm{WS}(t)dt = mg$$

Analyzed wingbeats from 75-cm flights

Although five flights per bird were analyzed to determine total leg and wing impulses for each 75-cm flight variation, only three flights per bird were selected for the analyses involving wingbeats and kinematics (Fig. 3, D to F, and figs. S7 and S8) because of differences in individual stroke patterns. The four parrotlets sometimes varied the number of strokes that they took before or after a bound, and in a few cases, they did not bound at all. To exclude kinematic or aerodynamic effects that may have resulted from preparation for a bound, we selected three flights for each bird in which it used the same wingbeat pattern (that is, no bounding, or the same number of wingbeats before and after a bound). For level flights, all four birds took at least three wingbeats before and after bounding (fig. S7A), so the second wingbeat from each bird was chosen as the "takeoff wingbeat," and the second to last wingbeat was chosen as the "landing wingbeat." These definitions also worked well for ascending flights (fig. S7B). For descending flights, the same definition was used for the "landing wingbeat," but the "takeoff wingbeat" was defined as the first wingbeat instead, because one bird frequently bounded after its second downstroke (fig. S7C). In our analysis of the relation between body angle and vertical impulse ratio (Fig. 3F and fig. S4A) and actuator disc area (fig. S4B), we only included full wingbeats (complete downstroke and upstroke), so final wingbeats before landing and wingbeats before a bound were excluded.

Downstroke impulse during level flights

To compare partial wingbeats used during 20-cm flights with the full wingbeats used during level, 40- and 75-cm flights, we calculated the impulse generated during the first downstroke of each flight variation. The averaged downstroke vertical impulse for 20-cm flights was 71 ± 38% bodyweight impulse (N = 4), where bodyweight impulse is calculated as $mg\Delta t_{\mathrm{DS}}$ (mg, bodyweight; Δt_{DS}, duration of downstroke). We analyzed five flights for each bird, but two flights were omitted because the bird did not flap its wings to reach the landing perch. The 20-cm downstroke impulse was roughly half that of longer flights; the first downstroke generated 143 ± 17% bodyweight impulse for 40-cm flights (N = 4, n = 5) and 135 ± 18% bodyweight impulse for 75-cm flights (N = 4, n = 3).

Mechanical energy model for foraging flight

We estimate the mechanical energy E needed for a bird to travel from perch to perch by summing the mechanical energy required by the legs during take-off, E_{legs}, with the mechanical energy required by the wings during flapping flight, E_{wings}. To determine how directing leg impulse affects the total required energy for a flight, we modeled E as a function of the takeoff angle θ

$$E(\theta) = E_{\mathrm{legs}}(\theta) + E_{\mathrm{wings}}(\theta) \quad (4)$$

As we will detail in the following sections, we separated each flight into three main phases: push-off, ballistic flight, and flapping flight. E_{legs} was calculated by applying a long jump model to determine the kinetic and potential energy changes during the push-off phase. The second phase, ballistic flight, was typically very brief and took place after toe-off and before the bird begins flapping. We determined flapping start times based on what parrotlets actually did for each flight variation, except for 20-cm flights, for which the jump range was first maximized before flapping flight began. The displacement during the ballistic flight phase is calculated from the takeoff velocity. The flapping flight time and velocity components for the flapping flight phase were then calculated on the basis of the remaining distance to the landing perch and average recorded flight velocities. The required wing energy E_{wings} is calculated from the flapping flight time and the power needed to support bodyweight and accelerate to and from the average flight speed.

Energy required by the legs during push-off

We began by modeling the bird's takeoff using the same approach corroborated in studies of human long jumps (*24*), where the jumper applies an average muscular force F_{m} over a push-off range l (the displacement of its center of mass during leg extension; fig. S9A). In these long jumps, F_{m} and l are independent of θ, but takeoff speed v_{TO} does depend on θ because a greater proportion of the muscular force must be used to counteract bodyweight. Less muscular force is thus available to overcome inertia and accelerate the body. This relation between v_{TO} and θ is given by (*24*)

$$v_{\mathrm{TO}}(\theta) = \sqrt{\frac{2F_{\mathrm{m}}l}{m} + v_{\mathrm{i}}^2 - 2gl\sin(\theta)} \quad (5)$$

where g is gravity and v_{i} is the speed of the center of mass at the start of push-off. The birds in our study started from rest on the takeoff perch (v_{i} = 0), and with $E_{\mathrm{legs}} = F_{\mathrm{m}}l$, we can express Eq. 5 as

$$v_{\mathrm{TO}}(\theta) = \sqrt{\frac{2E_{\mathrm{legs}}}{m} - 2gl\sin(\theta)} \quad (6)$$

or rearranging

$$E_{\mathrm{legs}} = \frac{1}{2}mv_{\mathrm{TO}}^2 + mgl\sin\theta \quad (7)$$

Note that Eq. 7 can also be derived directly from conservation of energy principles; energy required by the legs is used to change the bird's kinetic energy ($\Delta\mathrm{KE} = \frac{1}{2}mv_{\mathrm{TO}}^2$) and potential energy ($\Delta\mathrm{PE} = mgl\sin\theta$) during takeoff. We calculated E_{legs} for each flight variation using Eq. 7 with the average takeoff speeds and angles from our kinematic data (table S1). We estimated the push-off range as $l \approx 5.0$ cm based on the average displacement of the bird's eye during takeoff, again assuming that the bird's eye does not significantly move relative to its center of mass. We then set E_{legs} equal to its average across the 40- and 75-cm variations. Values calculated for each of these variations only differed by about 10% from this average, so we assume that E_{legs} is constant during all flights, with one exception: If the ballistic range predicted for a 20-cm flight exceeded the required distance to land on the perch, then E_{legs} is decreased until there is no more overshoot.

Displacements during the ballistic flight phase

Once airborne, a jumper can be treated as a projectile in free flight (*24*), so we model the time after push-off and before the wings begin flapping, Δt_{legs}, as ballistic flight. To find Δt_{legs}, we first found the average time between toe-off and the start of the first downstroke for ascending, level (40 and 75 cm), and descending flights. We then used a linear fit (R^2 = 0.88) to find Δt_{legs} as a function of the effective inclination $\tan^{-1}\frac{\Delta z}{\Delta x}$

$$\Delta t_{legs} = -0.0003\tan^{-1}\left(\frac{\Delta z}{\Delta x}\right) + 0.0101\,\mathrm{s} \tag{8}$$

The effects of air resistance are negligible given the low takeoff velocities of our birds (table S1). The horizontal and vertical displacements covered during the ballistic flight phase (Δx_{legs} and Δz_{legs}) can thus be calculated from traditional projectile motion equations

$$\Delta x_{legs}(\theta) = v_{TO,x}\Delta t_{legs} \tag{9a}$$

$$\Delta z_{legs}(\theta) = v_{TO,z}\Delta t_{legs} - \frac{1}{2}g\Delta t_{legs}^2 \tag{9b}$$

where $v_{TO,x}$ and $v_{TO,z}$ are the horizontal and vertical components, respectively, of the takeoff velocity from Eq. 6. Flapping flight was less consistently used for 20-cm flights (fig. S2), so for this distance, we modeled the maximal ballistic flight range based on jumping alone

$$\Delta x_{legs,20cm}(\theta) = \Delta x_{legs,\,max} = \frac{v_{TO}^2\sin(2\theta)}{g} \tag{10a}$$

$$\Delta z_{legs,20cm} = 0 \tag{10b}$$

$$\Delta t_{legs,20cm}(\theta) = \frac{\Delta x_{legs,20cm}}{v_{TO,x}} \tag{10c}$$

The displacements covered by the wings during flapping flight (Δx_{wings} and Δz_{wings}) must then make up the remaining distance to the final (landing) position (fig. S9B)

$$\Delta x_{wings} = \Delta x - \Delta x_{legs} \tag{11a}$$

$$\Delta z_{wings} = \Delta z - \Delta z_{legs} \tag{11b}$$

We estimated the total horizontal (Δx) and vertical (Δz) displacements of the bird's center of mass using the average displacement of the eye for each of the five flight variations (table S2).

Flapping flight time and average velocity components

Using the displacement that needs to be covered with flapping flight (Eq. 11), we can determine the flapping flight time Δt_{wings} and velocities. The average flight speed across all 75-cm flights was V_{avg} = 1.6 ± 0.1 m/s, so we assume that V_{avg} only varies with distance, not inclination or θ. The flapping flight time is then

$$\Delta t_{wings}(\theta) = \frac{\sqrt{\Delta x_{wings}^2 + \Delta z_{wings}^2}}{V_{avg}} \tag{12}$$

and the average horizontal (V_x) and vertical (V_z) flight velocities are

$$V_x(\theta) = \frac{\Delta x_{wings}}{\Delta t_{wings}} \tag{13a}$$

$$V_z(\theta) = \frac{\Delta z_{wings}}{\Delta t_{wings}} \tag{13b}$$

Energy required by wings during flapping flight

We now calculate E_{wings} as the sum of three components: the energy needed to support bodyweight during Δt_{wings}; the energy needed to accelerate to V_x and V_z from $v_{TO,x}$ and $v_{TO,z}$; and the energy needed to brake before landing. We calculate the average power needed to support bodyweight as the sum of inertial power $\bar{P}_{inert}$, profile power $\bar{P}_{pro}$, induced power $\bar{P}_{ind}$, and climb power $\bar{P}_{climb}$. On the basis of our velocity measurements (fig. S8), we assume that the bird accelerates to the average flight velocity during the first wingbeat and decelerates to a horizontal landing speed no greater than 1 m/s during the final two wingbeats (measured landing speed was 0.95 ± 0.09 m/s; table S1). Because the upstroke is relatively inactive, the power used to accelerate $\bar{P}_{accel}$ acts during one downstroke Δt_{DS}, and the power used to brake $\bar{P}_{brake}$ acts during two downstrokes. Thus, in summary, we calculate the energy the wings require as

$$E_{wings}(\theta) = \left(\overline{P_{inert}} + \overline{P_{pro}} + \overline{P_{ind}}(\theta) + \overline{P_{climb}}(\theta)\right)\Delta t_{wings} + \overline{P_{accel}}(\theta)\Delta t_{DS} + \overline{P_{brake}}(\theta)2\Delta t_{DS} \tag{14}$$

The equations used in the following sections are derived from quasi-steady aerodynamic theory, which is commonly applied in studies of flapping flight (*25*–*31*, *42*). Unlike steady-state assumptions, quasi-steady theories assume that aerodynamic forces result primarily from the instantaneous flow field produced throughout the wingbeat and can therefore vary in time because of changes in wing and body kinematics.

Profile power

The average profile power for flapping flight can be calculated by (*27*–*29*)

$$\bar{P}_{pro} = 2^*\frac{1}{2}\rho R_3^3 S\bar{C}_d\frac{1}{T}\int_0^T\left|\dot{\phi}\right|^3 dt \tag{15}$$

where R_3 is the third moment of area of the wing [for example, see the study of Kruyt *et al.* (*28*)], S is the area of a single wing, $\bar{C}_d$ is the average profile drag coefficient, T is the wingbeat period, and $\dot{\phi}$ is the stroke angle velocity. To estimate the geometric properties of the wing, we extracted an image of a fully extended wing from the ventral view of a parrotlet mid-flight. By dividing the wing into 20 equally spaced wing strips, we calculated R_3 = 0.0582 m, S = 0.0039 m^2, and a wing length r = 10 cm. The stroke angle velocity $\dot{\phi}$ was calculated by dividing the wingtip velocity by the wing length, where the wingtip velocity was derived from differentiating the tracked position of the wingtip during a level, 75-cm flight. Our profile drag coefficient estimate is $\bar{C}_d$ = 0.20, which is among the higher $\bar{C}_d$ values reported in the literature (*27*, *30*, *31*, *42*), and thus represents a more pessimistic estimate for our predicted energy requirements. We note that varying $\bar{C}_d$ from 0.01 (the minimum reported value) to 0.40 did not affect our predicted energy-minimizing takeoff angles by more than 1°.

Induced power

During flapping flight, the area swept out by the wings can be modeled as an actuator disc, for which the induced power (P_{ind}) is given by (*25*, *26*, *43*)

$$P_{ind} = \kappa F V_i \tag{16}$$

where κ is the induced power factor, which accounts for nonideal effects such as tip losses and nonuniform inflow (*43*); F is the aerodynamic force generated by the wings; and V_i is the induced velocity through the actuator disc. During axial flight (no forward velocity), the induced velocity is given by

$$V_{i,a} = \sqrt{\frac{F}{2\rho A_d}} \tag{17}$$

where ρ is the density of air, and A_d is the actuator disc area, the area swept out by the wings projected onto a plane normal to F. In forward flight at velocity V_∞ and angle of attack α (the angle between the actuator disc and V_∞), the induced velocity becomes (*44*)

$$V_i = \frac{V_{i,a}^2}{\sqrt{(V_\infty \cos(\alpha))^2 + (V_\infty \sin(\alpha) + V_i)^2}} \tag{18}$$

Given the slow average flight speeds ($V_\infty = 1.6 \pm 0.1$ m/s; $N = 4$, $n = 3$ for all 75-cm variations), the net stroke-averaged force generated by the flapping wings $\bar{F}$ is about equal to bodyweight ($\bar{F} = mg$) and directed mostly vertically. The actuator disc is oriented horizontally, and the average induced velocity is

$$\overline{V_i} \approx \frac{\overline{V_{i,a}}^2}{\sqrt{V_x^2 + (V_y + \overline{V_i})^2}} \tag{19}$$

Body pitch effects

The average induced power over a wingbeat increases when the total vertical impulse is generated more asymmetrically and is lowest when F remains constant throughout the wingbeat. This means that as the upstroke to downstroke impulse ratio increases (as vertical lift generation is distributed more evenly), the induced power decreases. P_{ind} also decreases with the actuator disc area. Thus, because both the impulse ratio and actuator disc area increase with body angle (Fig. 3F and fig. S4, A and B), the induced power decreases with body angle. To incorporate these effects, we modified Eqs. 16 and 17 so that the actuator disc area A_d and the induced power factor κ are both functions of β.

For the projected actuator disc area, we modeled $A_d(\beta)$ using the geometric relation

$$A_d(\beta) = S_d \cos\left(180° - (\beta + \beta_o)\right) \tag{20}$$

The area swept out by the wings, $S_d = \Phi r^2$, is held reasonably constant throughout the flight, as found for other species (*29*). We measured a peak-to-peak stroke amplitude of about $\Phi \approx 2.3$ rads (±0.6 rad; $N = 4$, $n = 3$ each for 75-cm, level flights). Stroke plane angle relative to the body angle remains relatively constant during pigeon flights (*45*); accordingly, the stroke plane in the parrotlet model is set at a constant offset β_o from the body angle. We estimated $\beta_o = 100°$ from our 75-cm, level flight videos ($\beta_o = 99.9 \pm 2.9°$; $N = 4$, $n = 3$). The projected disc area predicted by Eq. 20 fits well with our kinematic data (fig. S4B).

For the induced power factor, we set $\kappa(\beta) = \kappa_1 \kappa_2(\beta)$, where κ_1 is the original factor introduced in Eq. 16 to account for tip losses, and κ_2 is introduced to account for the uneven disc loading—the increase in the upstroke to downstroke impulse ratio across the flight. We set $\kappa_1 = 1.2$, following widely accepted aerodynamic models for bird flapping flight (*31*, *36*, *42*, *46*). To determine suitable values for κ_2, we first normalized average takeoff and landing wingbeat force traces (Fig. 3, D and E) so that the total vertical impulse would be equal to the bodyweight impulse (that is, the impulse if F was directed vertically and equal to bodyweight throughout the wingbeat). The wingbeat-averaged induced powers for the 75-cm flight variations were then compared with the induced power using an ideal (constant) force profile. For these calculations, we used Eq. 16 approximating V_i as the axial flight induced velocity $V_{i,a}$ (Eq. 17), and setting $\rho = 1.18$ kg/m^3 (density of air at 25°C; the average measured temperature during our experiments), $\kappa = \kappa_1 = 1.2$, and $A_d = S_d$. The induced power ratios of the takeoff force trace to the ideal force trace were 1.31, 1.30, and 1.27 for level, ascending, and descending flights, respectively, so we set $\kappa_2 \approx 1.3$ for takeoff wingbeats. The ratios of the landing force trace to the ideal force trace were 1.11, 1.14, and 1.15, so $\kappa_2 \approx 1.1$ for landing wingbeats. Given the reasonably linear correlation ($R^2 = 0.60$) between the impulse ratio and body angle (fig. S4A), we use a linear trend to model the relation between κ_2 and the body angle β; the average body angle across the three inclinations was 28° for takeoff wingbeats and 66° for landing wingbeats, so a line through these two points gives

$$\kappa_2 = \frac{1.1 - 1.3}{66 - 28}(\beta - 28°) + 1.3 \tag{21}$$

Finally, we calculate the average induced power to support bodyweight by averaging each flight parameter independently

$$\overline{P_{ind}} \approx \bar{\kappa} \bar{F} \overline{V_i} \tag{22}$$

To average $\kappa(\beta)$ and $V_i(\beta)$ with respect to time for each flight, we model β as a function of time. For simplicity, we modeled a linear increase in body angle over the total flight time ($\Delta t_{tot} = \Delta t_{legs} + \Delta t_{wings}$) for each flight variation (fig. S4C; $R^2 = 0.84$, 0.71, and 0.89 for level, ascending, and descending flights, respectively). The best-fit lines began at different body angles but converged to approximately 80° at the end of each flight. On the basis of these best-fit lines and observations from our flight videos, we treated the initial body angle β_i as a constant for each flight variation, determined by the effective inclination $\beta_i = \tan^{-1}\frac{\Delta z}{\Delta x}$. The body angle is thus modeled as

$$\beta(t) = \frac{80° - \beta_i}{\Delta t_{tot}} t + \beta_i \tag{23}$$

Climbing power

The final main flight power component, climb power, is the time rate of increase of potential energy (*43*). The average climb power required to maintain V_z is thus

$$\bar{P}_{climb} = \bar{F} V_z = mg V_z \tag{24}$$

Accelerating power

To find the induced and climb power needed to accelerate to the average flight velocities after ballistic flight, we first calculate the necessary horizontal impulse J_x and vertical impulse J_z

$$J_x(\theta) = m(V_x - v_{TO,x}) \tag{25a}$$

$$J_z(\theta) = \mathrm{m}(V_z - v_{TO,z}) \tag{25b}$$

On the basis of our velocity measurements, this impulse is generated during the first downstroke (for 75-cm flights, the time to reach the average flight velocity from the start of flapping ranged from about 0.5 to 0.7 wingbeats). The average force required to support bodyweight and accelerate to the average flight velocities is therefore

$$\overline{F_{accel}} = \sqrt{\left(\frac{J_x}{\Delta t_{DS}}\right)^2 + \left(\frac{J_z}{\Delta t_{DS}} + mg\right)^2} \tag{26}$$

The induced velocity $V_{i,accel}$ is then calculated from Eqs. 16 and 18 with $F = \overline{F_{accel}}$. Body angle during the accelerating wingbeat β_{accel} is calculated from Eq. 23, with $t = \Delta t_{legs}$, except for 20-cm flights; we found that the parrotlets tended to start from larger body angles for these "jumping" flights, so we used $\beta_{accel} = 60°$, the average body angle during their occasional wingbeats ($\beta = 60 \pm 6°$; $N = 4$). The actuator disc area becomes $A_{d,accel} = S_d \cos(\xi)$, where ξ is the angle between the stroke plane and the plane normal to the force vector $\xi = (\beta_{accel} + \beta_0) - \left(\tan^{-1}\frac{F_{accel,z}}{F_{accel,x}} + 90°\right)$. For accelerating wingbeats, we used $\beta_o = 97°$ based on the average for the first wingbeat during level, 75-cm flights ($\beta_o = 96.7 \pm 5.7°$; $N = 4$, $n = 3$). Isolating the power needed just for accelerating

$$\overline{P_{ind,accel}} \approx \kappa(\beta_{accel})\overline{F_{accel}}V_{i,accel} - P_{ind,steady} \tag{27}$$

$$\overline{P_{climb,accel}} \approx \overline{F_{accel}}V_z - P_{climb,steady} \tag{28}$$

where $P_{ind,steady}$ and $P_{climb,steady}$ are the average power components needed to support bodyweight from Eqs. 22 and 24, respectively. The accelerating power is then

$$\bar{P}_{accel} = \overline{P_{ind,accel}} + \overline{P_{climb,accel}} \tag{29}$$

We note that for 20-cm flights, $\bar{P}_{accel}$ may actually be used for braking instead of accelerating if the initial takeoff velocity is too high.

Braking power

On the basis of the velocity profiles, we assume that braking before landing is primarily in the horizontal direction to ensure a landing speed $v_{LD,x} \leq 1$m/s. If V_x is already below 1 m/s, as in the case of 20-cm flights, then no braking is used. For 75-cm flights, the time to reach $v_{LD,x}$ from the average flight speed ranged from about 1.4 to 1.8 wingbeats. Therefore, we model braking force F_{brake} during the final two downstrokes. The average braking force needed to reach the desired landing speed while supporting bodyweight is thus

$$\overline{F_{brake}} \approx \sqrt{\left(m\frac{v_{LD,x} - V_x}{2\Delta t_{DS}}\right)^2 + (mg)^2} \tag{30}$$

The same formulas used for accelerating power can then be applied to find power needed for braking

$$\bar{P}_{brake} = \overline{P_{ind,brake}} + \overline{P_{climb,brake}} \tag{31}$$

but with $\bar{F} = \overline{F_{brake}}$, and β evaluated halfway between the two downstrokes, at time $t = \Delta t_{tot} - 2.5\Delta t_{DS}$, with $\beta_o = 103°$ based on the average for the last two wingbeats during level, 75-cm flights ($\beta_o = 103.1 \pm 4.7°$, $N = 4$, $n = 3$).

Inertial power

To calculate inertial power, we assumed that work is only required to accelerate the wing because the vertebrate muscle is highly efficient when generating force to absorb energy (*29*, *33*, *47*). P_{inert} is then given by (*48*)

$$P_{inert} = 2\pi^2\Phi^2 f^3 I \tag{32}$$

where f is the wingbeat frequency and I is the inertia of a wing. We scaled mass and length measurements from two pairs of lovebird (*Agapornis*) wings to calculate I for the parrotlets using (*49*)

$$I = \sum_{i=1}^{n}\left(m_i d_i^2 + \frac{m_i w_i^2}{12}\right) \tag{33}$$

where m_i is the mass of wing strip i, d_i is the distance between the center of strip i and the shoulder joint, w_i is the width of strip i, and $n = 7$ is the number of strips.

Elastic storage has been identified as a mechanism for reducing inertial energy costs in terrestrial locomotion (*50*–*52*) and flapping insect flight (*29*, *53*, *54*). Small birds may also be able to make use of elastic storage in their muscle-tendon units (*48*). Although this mechanism has not been studied as well in birds, substantial elastic energy storage has been reported for the pigeon supracoracoideus (*55*) and is also likely used by hummingbirds (*56*). Furthermore, the intrinsic wing muscles of a bird wing often have short fibers and long tendons, which are characteristic of muscles suited for recovering elastic energy from their tendons (*57*). We therefore assume that parrotlets use elastic energy storage during their wingbeats such that inertial power requirements can be neglected for all but the first wingbeat. The total mechanical energy required by the wings thus becomes

$$E_{wings}(\theta) = \overline{P_{inert}}\,\Delta t_{WB} + \left(\overline{P_{pro}} + \overline{P_{ind}}(\theta) + \overline{P_{climb}}(\theta)\right)\Delta t_{wings} + \overline{P_{accel}}(\theta)\Delta t_{DS} + \overline{P_{brake}}(\theta)2\Delta t_{DS} \tag{34}$$

where Δt_{WB} is the wingbeat period.

Finally, we consider the case of zero elastic storage. Without recoil, $\overline{P_{inert}}$ contributes to energetic costs over the entire flapping flight time, so

$$E_{wings}(\theta) = \left(\overline{P_{inert}} + \overline{P_{pro}} + \overline{P_{ind}}(\theta) + \overline{P_{climb}}(\theta)\right)\Delta t_{wings} + \overline{P_{accel}}(\theta)\Delta t_{DS} + \overline{P_{brake}}(\theta)2\Delta t_{DS} \tag{35}$$

In Eqs. 34 and 35, if $\Delta t_{wings} \leq \Delta t_{WB}$, as in some 20-cm flights, then $\overline{P_{pro}}$ and $\overline{P_{inert}}$ are multiplied by Δt_{WB} instead. We show in fig. S10 that while assuming zero elastic storage would increase total mechanical energy costs, it does not change the energy-minimizing takeoff angles. We also note that the "zero elastic storage" assumption is very pessimistic; parrotlets use tip-reversal upstrokes, which greatly minimize the inertial work required. In addition, Hedrick *et al.* (*33*) found that cockatiels, also arboreal Psittaciformes, use nearly all wing kinetic energy toward aerodynamic force generation. This finding validates a common assumption in the literature (*31*, *32*, *58*) that inertial power requirements during the downstroke do not significantly increase energetic costs.

Predicted mechanical energy requirements

The results of applying this mechanical energy model corroborated from the parrotlet flight data are shown in Fig. 4A, and the relevant parameters and predicted energy-minimizing takeoff angles are included in table S2.

Protowing model

We next simplify our foraging flight model to show the potential increase in range and corresponding energetic cost from extending a long jump with a single proto-wingbeat (Fig. 4B). We first simulated the range gain and energetic cost trade-off for a single parrotlet proto-wingbeat, which models the fledgling stage. We then repeated our single wingbeat simulation using estimates for mass, wing length, wing area, wingbeat frequency, and hindlimb length from the study by Dececchi *et al.* (*35*) for four bird antecedents: *Archaeopteryx*, *Microraptor*, *Caudipteryx*, and *Protarchaeopteryx* (table S4).

We model takeoff as before, calculating the takeoff velocity with Eq. 6. For bird antecedents, we assumed that hindlimb length is equal to 80% of the push-off range. This assumption is based on measured hindlimb lengths of parrotlets (5.8 ± 0.1 cm; $N = 3$) compared to their push-off range of about 5 cm, that is, 5 cm/6 cm ≈ 80%. We note that our model results are robust to significant changes in this assumption. For example, changing the push-off range from 100 to 50% of hindlimb length results in an 8 to 11% decrease in the added range results across all bird antecedents. To calculate E_{legs}, we used the takeoff velocities reported by Dececchi *et al.* (*35*) (predicted on the basis of extant taxa leaping capabilities) for $\theta = 30°$. We then identify the θ that maximizes the horizontal jump range when no wingbeat is used (x_0).

Next, given the limited forelimb abduction capabilities of theropods (*35*), we simulate the proto-wingbeat as a single downstroke, with peak-to-peak stroke amplitude Φ restricted to 70°. For simplicity, this downstroke generates a constant force F_{DS} to support a fraction of bodyweight mg. The net vertical acceleration during the downstroke is then

$$a_{z,DS}(\theta) = F_{DS}/m - g \tag{36}$$

We simulated downstrokes that generate vertical lift equal to 1 to 100% of bodyweight. The single downstroke starts at time t_o after toe-off and is followed by ballistic flight until the bird returns to its initial height, which defines the horizontal range. For each weight support value, we determine the takeoff angle that maximizes the horizontal long jump range x and then calculate the percent increase from x_0 (Eq. 10a) as follows: $\Delta X = \frac{x - x_0}{x_0} \times 100\%$. As we show in the following derivation and in the simulated results for a parrotlet in fig. S5A, delaying the timing of the downstroke decreases x. Thus, by optimizing takeoff angle and initiating the downstroke immediately after toe-off, we can compare the maximum horizontal range of both the wing-assisted and nonassisted jump.

To find the corresponding mechanical energy cost for introducing the partial wingbeat (E_{wings}), we sum the profile power (Eq. 15), induced power (Eq. 16), climb power (Eq. 24), and inertial power (Eq. 32) needed to supply F_{DS} during the downstroke. For these short parrotlet long jumps, we apply the common assumption that inertial power can be neglected when calculating aerodynamic power requirements during the downstroke, because nearly all wing kinetic energy is used in producing aerodynamic force (*31*–*33*, *59*). On the other hand, the wingbeats of bird antecedents were much less effective at aerodynamic force production, and it is unclear whether antecedents benefited from elastic recoil or other inertial power mitigating mechanisms, so we include inertial power when estimating their power requirements. To do so, we estimated wing inertia with the scaling law corroborated for birds by Berg and Rayner (*49*) as follows: $I = 0.00194m^{1.953}$. To calculate profile power, we modeled their wings as semielliptical to calculate R_3 and their wingbeat as sinusoidal to calculate $\dot{\phi}$. We use the same conservative estimate for $\overline{C_d}$ as with the parrotlets. Although the profile power term requires several assumptions, it is generally much smaller than the induced or inertial power terms. Therefore, we assume the same $\overline{C_d}$ value across all theropods, so the comparisons between them are unaffected. For induced power, we use $\kappa = 1.2$ as in other bird flapping flight studies (*31*, *36*, *42*, *46*), and we use our parrotlet data to determine the stroke plane angle to calculate actuator disc area. We use the average velocity during the downstroke to calculate induced and climb power. Finally, the percent increase in energy cost with the additional downstroke is calculated as follows: $\frac{E_{legs}+E_{wings}}{E_{legs}} \times 100\%$.

To limit simulated proto-wingbeats to those that are physiologically plausible, we assumed that bird antecedents were capable of generating no more than the maximum muscle mass–specific power required by parrotlets. To calculate this threshold, we divided the aerodynamic power required for a parrotlet to generate 200% bodyweight impulse during a downstroke (so 100% weight support averaged over a full wingbeat) by their flight muscle mass. We set parrotlet flight muscle mass equal to 16% of body mass, based on measurements made with three sacrificed parrotlets that were not used in this study (pectoralis mass of 16.0 ± 0.8% body mass; $N = 3$). This gave a wingbeat-averaged power normalized by pectoralis mass of 317 W/kg. We note that because flapping stops after the downstroke in our simulated flights (that is, no upstroke is made) and the downstroke duration is half of a full wingbeat, then the required power averaged over a full wingbeat is half of the downstroke power. The power output of 317 W/kg is likely an overestimation given our conservative estimate for the profile drag coefficient; if we use $\overline{C_d} = 0.02$ instead, as in previous studies (*31*–*33*, *59*), then the maximum power output is 262 W/kg. Both values fall within estimates of aerodynamic power requirements that have been reported in the bird flight literature, which range from below 100 W/kg to over 500 W/kg (*31*, *32*, *55*, *59*, *60*). To calculate mass-specific power for the bird antecedents, following Dececchi *et al.* (*35*), we assumed that their flight muscle mass is 10% of their body mass, which is a reasonable assumption for *Archaeopteryx* (*61*) but is likely an overestimation for the larger antecedents (*35*). On the basis of a maximum muscle mass–specific burst output of 317 W/kg (and using $\overline{C_d} = 0.2$), we calculated that the associated maximal wingbeat-averaged weight support that bird antecedents were capable of are 6% aerodynamic bodyweight support for *Caudipteryx*, 11% for

Protarchaeopteryx, 31% for *Microraptor*, and 43% for *Archaeopteryx*. Although the values for the non-avian theropods are likely an overestimation, those of the smaller bird antecedents agree reasonably well with values reported by Dececchi *et al.* (*35*).

How the long jump range increases with downstroke weight support

The percent increase in proto-wingbeat–assisted long jump range ΔX is a function of takeoff velocity and angle

$$\Delta X = \frac{x - x_0}{x_0} * 100 = 100\frac{x}{x_0} - 100 = 100\frac{v_{TO,x}\, t_f}{x_0} - 100$$
$$= 100\frac{v_{TO}\cos(\theta_2)}{v_{TO}^2 2\sin(\theta_1)\cos(\theta_1)/g} t_f - 100 \approx \frac{50g}{v_{TO}\sin(\theta_1)} t_f - 100$$

where t_f is the flight time, θ_2 is the optimal takeoff angle for the wing-assisted jump, and θ_1 is the optimal takeoff angle for the nonassisted jump. In the final step above, we assume $\cos(\theta_1) \approx \cos(\theta_2)$ because these angles are always within 1° of each other and taking the cosine makes these differences irrelevant. Noting that $v_{TO}\sin(\theta_1) = v_{TO,z}$, we can express ΔX as

$$\Delta X = \frac{50g}{v_{TO,z}} t_f - 100 \tag{37}$$

If the downstroke is applied at time t_o after takeoff, then the vertical position is given by

$$z = \int_0^{t_o} v_{TO,z} - gt\,dt + \int_{t_o}^{t_{DS}+t_o} (v_{TO,z} - gt_o) + a_{z,DS}(t - t_o)\,dt$$
$$+ \int_{t_{DS}+t_o}^{t_f} (v_{TO,z} - gt_o) + a_{z,DS}t_{DS} - g\big(t - (t_{DS} + t_o)\big)\,dt$$
$$= -\frac{1}{2}(a_{z,DS} + g)t_{DS}^2 - (a_{z,DS} + g)t_{DS}t_o + v_{TO,z}t_f$$
$$+ (a_z + g)t_{DS}t_f - \frac{1}{2}gt_f^2$$

To find t_f, we solve for when the vertical position returns to zero

$$\frac{1}{2}gt_f^2 - \left[v_{TO,z} + (a_z + g)t_{DS}\right]t_f + (a_z + g)t_{DS}\left(\frac{1}{2}t_{DS} + t_o\right) = 0$$

or substituting in $a_{z,DS} = \frac{F_{DS}}{m} - g$

$$\frac{1}{2}gt_f^2 - \left[v_{TO,z} + \frac{F_{DS}}{m}t_{DS}\right]t_f + \frac{F_{DS}}{m}t_{DS}\left(\frac{1}{2}t_{DS} + t_o\right) = 0 \tag{38}$$

We can now solve this quadratic equation for the time of flight t_f

$$t_f = \frac{v_{TO,z}}{g} + \frac{F_{DS}t_{DS}}{mg}$$
$$+ \left(\frac{v_{TO,z}}{g}\right)\sqrt{1 + \frac{2F_{DS}t_{DS}}{mv_{TO,z}} + \left(\frac{F_{DS}t_{DS}}{mv_{TO,z}}\right)^2 - \frac{F_{DS}t_{DS}^2 g}{mv_{TO,z}} - \frac{2gF_{DS}t_{DS}t_o}{mv_{TO,z}^2}}$$

Applying a first-order approximation for the square root, that is, $\sqrt{1+x} \approx 1 + \frac{x}{2}$, we obtain

$$t_f \approx 2\frac{v_{TO,z}}{g} + 2\frac{F_{DS}t_{DS}}{mg} + \frac{1}{2}\frac{F_{DS}^2 t_{DS}^2}{m^2 g v_{TO,z}} - \frac{1}{2}\frac{F_{DS}t_{DS}^2}{mv_{TO,z}} - \frac{F_{DS}t_{DS}t_o}{mv_{TO,z}}$$

Substituting this result into Eq. 37, we get the linearized long jump range extension

$$\Delta X \approx \frac{50g}{v_{TO,z}}\left(2\frac{v_{TO,z}}{g} + 2\frac{F_{DS}t_{DS}}{mg} + \frac{1}{2}\frac{F_{DS}^2 t_{DS}^2}{m^2 g v_{TO,z}} - \frac{1}{2}\frac{F_{DS}t_{DS}^2}{mv_{TO,z}} - \frac{F_{DS}t_{DS}t_o}{mv_{TO,z}}\right)$$
$$-100 = 100\frac{F_{DS}t_{DS}}{mv_{TO,z}}\left(1 - \frac{gt_o}{2v_{TO,z}} + \frac{F_{DS}t_{DS}}{4mv_{TO,z}} - \frac{gt_{DS}}{4v_{TO,z}}\right) \tag{39}$$

We can now clearly see that increasing t_o will decrease ΔX, so to maximize ΔX, we set $t_o = 0$.

With $t_o = 0$, the first term in the parentheses in Eq. 39 dominates, so we can further simplify this expression to

$$\Delta X \approx \frac{F_{DS}t_{DS}}{mv_{TO,z}} * 100$$

Finally, we can rewrite the equation for ΔX in terms of the percent bodyweight impulse per wingbeat J_{WB}, which we plot on the x axis in Fig. 4B. Using $F_{DS} = \frac{2J_{WB}}{100}mg$, we get

$$\Delta X \approx \frac{2gt_{DS}}{v_{TO,z}}J_{WB}\left(1 - \frac{gt_o}{2v_{TO,z}} + \frac{gt_{DS}}{2v_{TO,z}}\left(\frac{J_{WB}}{100} - \frac{1}{2}\right)\right)$$

and for $t_o = 0$

$$\Delta X \approx \frac{2gt_{DS}}{v_{TO,z}}J_{WB}$$

This linearization predicts the results of our simulation well (fig. S6), with a maximum percent difference ranging from only 8% (parrotlets) to 14% (*Caudipteryx*).

How wingbeat timing affects the power required to jump a fixed distance

We next determine how the downstroke weight support required for extending a jump by a fixed amount varies with wingbeat timing. The flight time t_f can be directly calculated from the total long jump range x as $t_f = \frac{x}{v_{TO,x}}$. We can therefore use Eq. 38 to solve for the downstroke impulse needed to reach x

$$F_{DS} = \frac{m\left(v_{TO,z}t_f - \frac{1}{2}g\,t_f^2\right)}{\frac{1}{2}t_{DS}^2 + t_{DS}t_o - t_{DS}t_f} \tag{40}$$

Using this equation, we find that the required downstroke weight support increases monotonically with the time that elapses between toe-off and the start of the downstroke t_o (fig. S5B). Aerodynamic power increases with downstroke weight support, so the power required to reach x also increases with t_o (fig. S5C). To gauge these wingbeat timing effects for both parrotlets and bird antecedents (fig. S5, B and C), we simulated proto-wingbeats that would provide an increase in the long jump range of 5%. We chose a 5% long jump extension, because it is feasible for all bird antecedents that we considered (Fig. 4B).

SUPPLEMENTARY MATERIALS

Supplementary material for this article is available at http://advances.sciencemag.org/cgi/content/full/3/5/e1603041/DC1

fig. S1. Key components of the AFP.

fig. S2. Inconsistent weight support during 20-cm jumping flights.
fig. S3. Horizontal takeoff and landing impulses.
fig. S4. Body angle correlations and changes during flight.
fig. S5. Effect of proto-wingbeat timing on distance and power required for a long jump.
fig. S6. Linear approximation for the long-jump range versus wingbeat impulse.
fig. S7. Representative force traces of individuals during 75-cm flights.
fig. S8. Velocity components during flight.
fig. S9. Key parameters used in modeling bird foraging flights.
fig. S10. Mechanical energy model results assuming zero elastic storage.
table S1. Takeoff and landing velocity data from Fig. 3 (A and B).
table S2. Mechanical energy model input parameter values and predictions for foraging flight.
table S3. Time rate of change of the tau function ($\dot{\tau}$).
table S4. Bird antecedent parameters from Dececchi *et al.* (*35*) used in the protowing model.
movie S1. In vivo weight support recording of a Pacific parrotlet during level, 20-cm flight.
movie S2. In vivo weight support recording of a Pacific parrotlet during level, 40-cm flight.
movie S3. In vivo weight support recording of a Pacific parrotlet during level, 75-cm flight.
movie S4. In vivo weight support recording of a Pacific parrotlet during ascending (+20°, 75-cm flight.
movie S5. In vivo weight support recording of a Pacific parrotlet during descending (−20°, 75-cm flight.

REFERENCES AND NOTES

1. S. K. Robinson, R. T. Holmes, Foraging behavior of forest birds: The relationships among search tactics, diet, and habitat structure. *Ecology* **63**, 1918–1931 (1982).
2. B. A. Maurer, Energetics of avian foraging, in *Avian Energetics and Nutritional Ecology*, C. Carey, Ed. (Chapman & Hall, 1996), pp. 250–279.
3. S. Chatterjee, *The Rise of Birds* (Johns Hopkins Univ. Press, ed. 2, 2015).
4. G. Caple, R. P. Balda, W. R. Willis, The physics of leaping animals and the evolution of preflight. *Am. Nat.* **121**, 455–476 (1983).
5. J. P. Garner, G. K. Taylor, A. L. R. Thomas, On the origins of birds: The sequence of character acquisition in the evolution of avian flight. *Proc. R. Soc. B Biol. Sci.* **266**, 1259–1266 (1999).
6. U. M. Norberg, Evolution of vertebrate flight: An aerodynamic model for the transition from gliding to active flight. *Am. Nat.* **126**, 303–327 (1985).
7. J. M. V. Rayner, The evolution of vertebrate flight. *Biol. J. Linn. Soc.* **34**, 269–287 (1988).
8. R. O. Prum, J. S. Berv, A. Dornburg, D. J. Field, J. P. Townsend, E. M. Lemmon, A. R. Lemmon, A comprehensive phylogeny of birds (Aves) using targeted next-generation DNA sequencing. *Nature* **526**, 569–573 (2015).
9. A. Grajal, Structure and function of the digestive tract of the Hoatzin (*Opisthocomus hoazin*): A folivorous bird with foregut fermentation. *Auk* **112**, 20–28 (1995).
10. F. H. Heppner, J. G. T. Anderson, Leg thrust important in flight take-off in the pigeon. *J. Exp. Biol.* **114**, 285–288 (1985).
11. R. Bonser, J. Rayner, Measuring leg thrust forces in the common starling. *J. Exp. Biol.* **199**, 435–439 (1996).
12. R. H. C. Bonser, A. P. Norman, J. M. V. Rayner, Does substrate quality influence take-off decisions in Common Starlings? *Funct. Ecol.* **13**, 102–105 (1999).
13. P. Green, P. Cheng, Variation in kinematics and dynamics of the landing flights of pigeons on a novel perch. *J. Exp. Biol.* **201**, 3309–3316 (1998).
14. R. H. Bonser, Branching out in locomotion: The mechanics of perch use in birds and primates. *J. Exp. Biol.* **202**, 1459–1463 (1999).
15. P. Provini, B. W. Tobalske, K. E. Crandell, A. Abourachid, Transition from leg to wing forces during take-off in birds. *J. Exp. Biol.* **4**, 4115–4124 (2012).
16. P. Provini, B. W. Tobalske, K. E. Crandell, A. Abourachid, Transition from wing to leg forces during landing in birds. *J. Exp. Biol.* **217**, 2659–2666 (2014).
17. K. D. Earls, Kinematics and mechanics of ground take-off in the starling Sturnis vulgaris and the quail Coturnix coturnix. *J. Exp. Biol.* **203**, 725–739 (2000).
18. B. W. Tobalske, D. L. Altshuler, D. R. Powers, Take-off mechanics in hummingbirds (Trochilidae). *J. Exp. Biol.* **207**, 1345–1352 (2004).
19. I. G. Ros, L. C. Bassman, M. A. Badger, A. N. Pierson, A. A. Biewener, Pigeons steer like helicopters and generate down- and upstroke lift during low speed turns. *Proc. Natl. Acad. Sci. U.S.A.* **108**, 19990–19995 (2011).
20. J. Lind, U. Kaby, S. Jakobsson, Split-second escape decisions in blue tits (*Parus caeruleus*). *Naturwissenschaften* **89**, 420–423 (2002).
21. D. Lentink, A. F. Haselsteiner, R. Ingersoll, *In vivo* recording of aerodynamic force with an aerodynamic force platform: From drones to birds. *J. R. Soc. Interface* **12**, 20141283 (2015).
22. M. H. Dickinson, C. T. Farley, R. J. Full, M. A. R. Koehl, R. Kram, S. Lehman, How animals move: An integrative view. *Science* **288**, 100–106 (2000).
23. J. P. Swaddle, E. V. Williams, J. M. V. Rayner, The effect of simulated flight feather moult on escape take-off performance in starlings. *J. Avian Biol.* **30**, 351–358 (1999).
24. M. Wakai, N. P. Linthorne, Optimum take-off angle in the standing long jump. *Hum. Mov. Sci.* **24**, 81–96 (2005).
25. C. J. Pennycuick, Power requirements for horizontal flight in the pigeon *Columbia Livia*. *J. Exp. Biol.* **49**, 527–555 (1968).
26. F. T. Muijres, G. R. Spedding, Y. Winter, A. Hedenström, Actuator disk model and span efficiency of flapping flight in bats based on time-resolved PIV measurements. *Exp. Fluids* **51**, 511–525 (2011).
27. U. M. Norberg, *Vertebrate Flight: Mechanics, Physiology, Morphology, Ecology and Evolution* (Springer-Verlag, 1990).
28. J. W. Kruyt, E. M. Quicazán-Rubio, G. F. van Heijst, D. L. Altshuler, D. Lentink, Hummingbird wing efficacy depends on aspect ratio and compares with helicopter rotors. *J. R. Soc. Interface* **11**, 570–581 (2014).
29. C. P. Ellington, The aerodynamics of hovering insect flight. VI. Lift and power requirements. *Philos. Trans. R. Soc. Lond. B Biol. Sci.* **305**, 145–181 (1984).
30. J. M. V. Rayner, A vortex theory of animal flight. Part 2. The forward flight of birds. *J. Fluid Mech.* **91**, 731–763 (1979).
31. B. W. Tobalske, T. L. Hedrick, K. P. Dial, A. A. Biewener, Comparative power curves in bird flight. *Nature* **421**, 363–366 (2003).
32. G. N. Askew, R. L. Marsh, C. P. Ellington, The mechanical power output of the flight muscles of blue-breasted quail (*Coturnix chinensis*) during take-off. *J. Exp. Biol.* **204**, 3601–3619 (2001).
33. T. L. Hedrick, J. R. Usherwood, A. A. Biewener, Wing inertia and whole-body acceleration: An analysis of instantaneous aerodynamic force production in cockatiels (*Nymphicus hollandicus*) flying across a range of speeds. *J. Exp. Biol.* **207**, 1689–1702 (2004).
34. D. Evangelista, S. Cam, T. Huynh, I. Krivitskiy, R. Dudley, Ontogeny of aerial righting and wing flapping in juvenile birds. *Biol. Lett.* **10**, 20140497 (2014).
35. T. A. Dececchi, H. C. E. Larsson, M. B. Habib, The wings before the bird: An evaluation of flapping-based locomotory hypotheses in bird antecedents. *PeerJ* **4**, e2159 (2016).
36. C. J. Pennycuick, Muscles as engines, in *Modelling the Flying Bird* (Elsevier Science, 2008), pp. 161–207.
37. M. S. Y. Lee, A. Cau, D. Naish, G. J. Dyke, Sustained miniaturization and anatomical innovation in the dinosaurian ancestors of birds. *Science* **345**, 562–566 (2014).
38. J. Forshaw, *Parrots of the World* (Princeton Univ. Press, 2010).
39. T. L. Hedrick, Software techniques for two- and three-dimensional kinematic measurements of biological and biomimetic systems. *Bioinspir. Biomim.* **3**, 034001 (2008).
40. D. N. Lee, P. E. Reddish, D. T. Rand, Aerial docking by hummingbirds. *Naturwissenschaften* **78**, 526–527 (1991).
41. D. Lee, M. N. O. Davies, P. Green, F. R. Van Der Weel, Visual control of velocity of approach by pigeons when landing. *J. Exp. Biol.* **180**, 85–104 (1993).
42. C. R. Morris, G. N. Askew, Comparison between mechanical power requirements of flight estimated using an aerodynamic model and in vitro muscle performance in the cockatiel (*Nymphicus hollandicus*). *J. Exp. Biol.* **213**, 2781–2787 (2010).
43. J. G. Leishman, *Principles of Helicopter Aerodynamics* (Cambridge Univ. Press, 2006).
44. H. Glauert, Airplane propellers, in *Aerodynamic Theory*, W. F. Durand, Ed. (Springer, 1935), pp. 169–360.
45. A. M. Berg, A. A. Biewener, Wing and body kinematics of takeoff and landing flight in the pigeon (*Columba livia*). *J. Exp. Biol.* **213**, 1651–1658 (2010).
46. G. N. Askew, D. J. Ellerby, The mechanical power requirements of avian flight. *Biol. Lett.* **3**, 445–448 (2007).
47. P. Chai, R. Dudley, Limits to vertebrate locomotor energetics suggested by hummingbirds hovering in heliox. *Nature* **377**, 722–725 (1995).
48. R. M. Alexander, *Principles of Animal Locomotion* (Princeton Univ. Press, 2013).
49. C. Berg, J. Rayner, The moment of inertia of bird wings and the inertial power requirement for flapping flight. *J. Exp. Biol.* **198**, 1655–1664 (1995).
50. R. V. Baudinette, A. A. Biewener, Young wallabies get a free ride. *Nature* **395**, 653–654 (1998).
51. T. J. Roberts, R. L. Marsh, P. G. Weyand, C. R. Taylor, Muscular force in running turkeys: The economy of minimizing work. *Science* **275**, 1113–1115 (1997).
52. A. A. Biewener, Muscle function in vivo: A comparison of muscles used for elastic energy savings versus muscles used to generate mechanical power. *Am. Zool.* **38**, 703–717 (1998).
53. M. H. Dickinson, J. R. Lighton, Muscle efficiency and elastic storage in the flight motor of Drosophila. *Science* **268**, 87–90 (1995).
54. R. M. Alexander, *Elastic Mechanisms in Animal Movement* (Cambridge Univ. Press, 1988).
55. B. W. Tobalske, A. A. Biewener, Contractile properties of the pigeon supracoracoideus during different modes of flight. *J. Exp. Biol.* **211**, 170–179 (2008).
56. P. Chai, R. Dudley, Maximum flight performance of hummingbirds: Capacities, constraints, and trade-offs. *Am. Nat.* **153**, 398–411 (1999).
57. A. A. Biewener, Muscle function in avian flight: Achieving power and control. *Philos. Trans. R. Soc. Lond. B Biol. Sci.* **366**, 1496–1506 (2011).
58. C. J. Pennycuick, Wingbeat frequency of birds in steady cruising flight: New data and improved predictions. *J. Exp. Biol.* **199**, 1613–1618 (1996).

59. T. L. Hedrick, B. W. Tobalske, A. A. Biewener, How cockatiels (*Nymphicus hollandicus*) modulate pectoralis power output across flight speeds. *J. Exp. Biol.* **206**, 1363–1378 (2003).
60. B. E. Jackson, K. P. Dial, Scaling of mechanical power output during burst escape flight in the Corvidae. *J. Exp. Biol.* **214**, 452–461 (2011).
61. J. R. Speakman, Flight capabilities in archaeopteryx. *Evolution* **47**, 336–340 (1993).

Acknowledgments: We thank A. F. Haselsteiner, R. Ingersoll, D. B. Quinn, and B. Hightower for their help in this study. **Funding:** This work was supported by NSF Faculty Early Career Development (CAREER) Award 1552419, the Office of Naval Research Multidisciplinary University Research Initiative grant N00014-10-1-0951, and the King Abdulaziz City for Science and Technology Center of Excellence for Aeronautics and Astronautics at Stanford. D.D.C. was supported by a Stanford Graduate Fellowship and a National Defense Science and Engineering Graduate Fellowship. **Author contributions:** D.D.C. collected and analyzed data. D.D.C. and D.L. designed the study, interpreted the findings, and wrote the paper. **Competing interests:** The authors declare that they have no competing interests. **Data and materials availability:** All data needed to evaluate the conclusions in the paper are present in the paper and/or the Supplementary Materials. Additional data related to this paper may be requested from the authors.

Submitted 2 December 2016
Accepted 15 March 2017
Published 17 May 2017
10.1126/sciadv.1603041

Citation: D. D. Chin, D. Lentink, How birds direct impulse to minimize the energetic cost of foraging flight. *Sci. Adv.* **3**, e1603041 (2017).

How birds direct impulse to minimize the energetic cost of foraging flight
Diana D. Chin and David Lentink (May 17, 2017)
Sci Adv 2017, 3:.
doi: 10.1126/sciadv.1603041

Science Advances

AAAS

advances.sciencemag.org/cgi/content/full/3/5/e1603041/DC1

Supplementary Materials for

How birds direct impulse to minimize the energetic cost of foraging flight

Diana D. Chin and David Lentink

Published 17 May 2017, *Sci. Adv.* **3**, e1603041 (2017)
DOI: 10.1126/sciadv.1603041

The PDF file includes:

Other Supplementary Material for this manuscript includes the following:
(available at advances.sciencemag.org/cgi/content/full/3/5/e1603041/DC1)

- movie S1 (.mp4 format). In vivo weight support recording of a Pacific parrotlet during level, 20-cm flight.
- movie S2 (.avi format). In vivo weight support recording of a Pacific parrotlet during level, 40-cm flight.

- movie S3 (.mp4 format). In vivo weight support recording of a Pacific parrotlet during level, 75-cm flight.
- movie S4 (.mp4 format). In vivo weight support recording of a Pacific parrotlet during ascending (+20°), 75-cm flight.
- movie S5 (.mp4 format). In vivo weight support recording of a Pacific parrotlet during descending (−20°), 75-cm flight.

Supplementary Figures

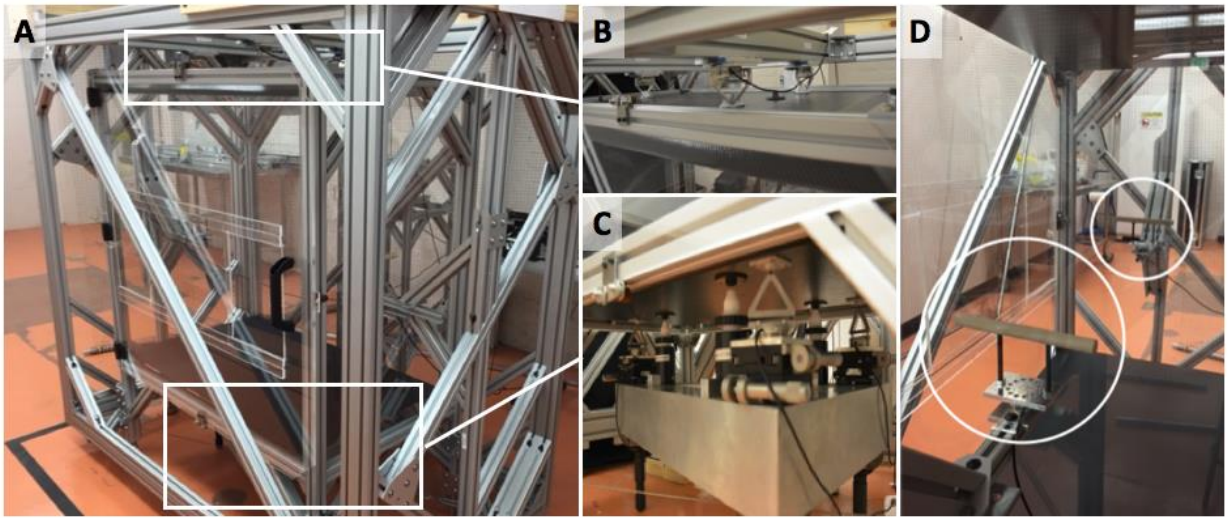

fig. S1. Key components of the AFP. All flights were recorded inside this aerodynamic force platform to capture the complete transfer of vertical impulse from the legs and wings during each flight. (**A**) Photo of the full setup, including the internal flight chamber, the top force plate and external structure, and the bottom plate. (**B**) The top plate is attached to the external structure via statically determined contact points with 3 force sensors. (**C**) The bottom plate is supported in a statically determined manner on three force sensors fixed to a supporting base. (**D**) Instrumented perches inside the setup measure both vertical and horizontal takeoff and landing forces.

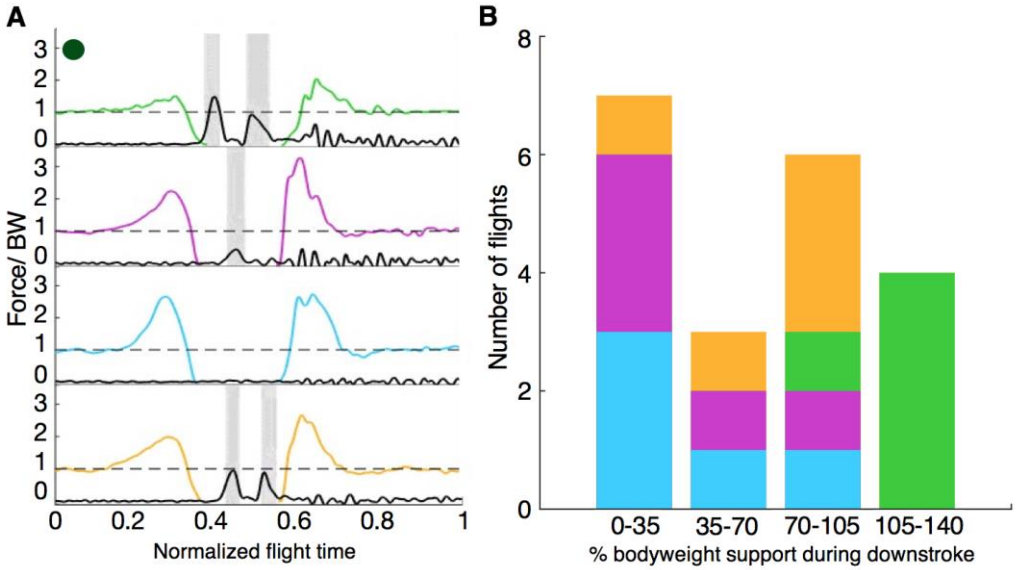

fig. S2. Inconsistent weight support during 20-cm jumping flights. (**A**) Representative 20 cm flights from all four birds show individual variation in timing and magnitude of wing contributions. Black lines show vertical forces generated by the wings, and colored lines show vertical leg forces during takeoff and landing. Gray shaded regions denote downstrokes. (**B**) Histogram showing the variation in vertical impulse generated during the first downstroke of 20

cm flights (*N=4, n=5*). Flights with no wingbeats were counted as having no bodyweight support. Colors correspond to the four birds represented in (A). The upper limit of vertical impulse generated by these partial wingbeats is about 135% bodyweight support. This maximal value corresponds roughly to the average vertical impulse of a full downstroke (see "Downstroke impulse during level flights"). Wing contributions during 20 cm flights thus vary from zero to full wingbeat based weight support.

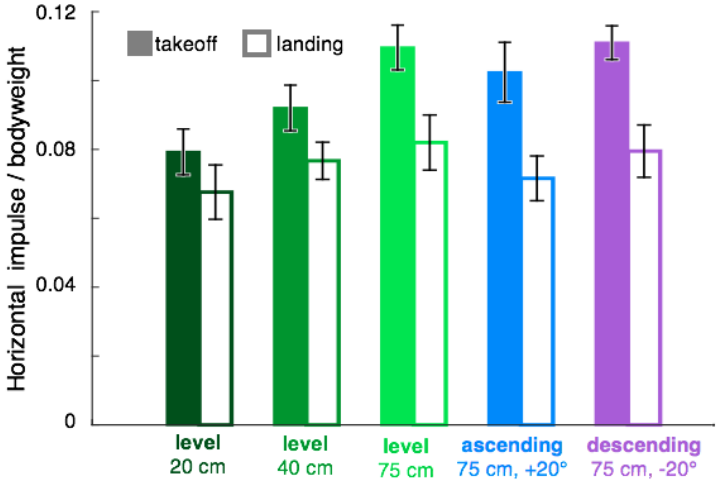

fig. S3. Horizontal takeoff and landing impulses. Parrotlets use their legs to generate significant horizontal impulse during takeoff (solid bars) and landing (open bars) across all flight variations. Horizontal takeoff impulse increased somewhat with distance as birds used their legs to accelerate to higher flight velocities. On the other hand, horizontal landing impulses remained relatively similar across different flight variations, because parrotlets consistently relied on their legs to come to a complete stop. Bars show mean ± std. dev. for *N=4* birds, *n=5* flights each.

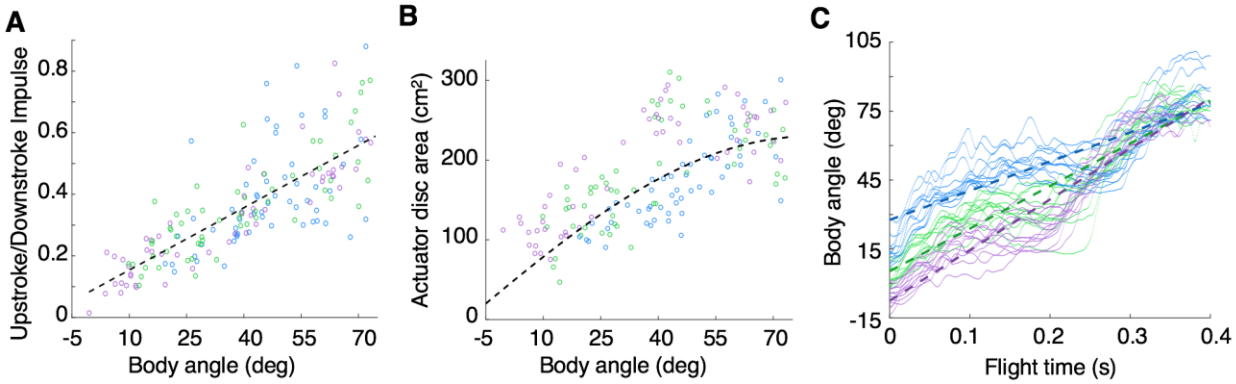

fig. S4. Body angle correlations and changes during flight. Increasing body angle is correlated with (**A**) an increase in the upstroke to downstroke vertical impulse ratio, and (**B**) an increase in the actuator disc area. (**C**) Parrotlets increased their body angle from near-horizontal to near-vertical orientations during flight across all inclinations. All panels show data from *N*=4 birds, *n*=3 flights each (see *Analyzed wingbeats from 75 cm flights*) per variation (green = level, blue = ascending, purple = descending). In the mechanical energy model, a linear trend was used to

model the vertical impulse ratio increase with body angle (dashed line in A), and a geometric relation (Eq. 17, dashed line in B) was used to represent the correlation between actuator disc area and body angle (see *Mechanical energy model*).

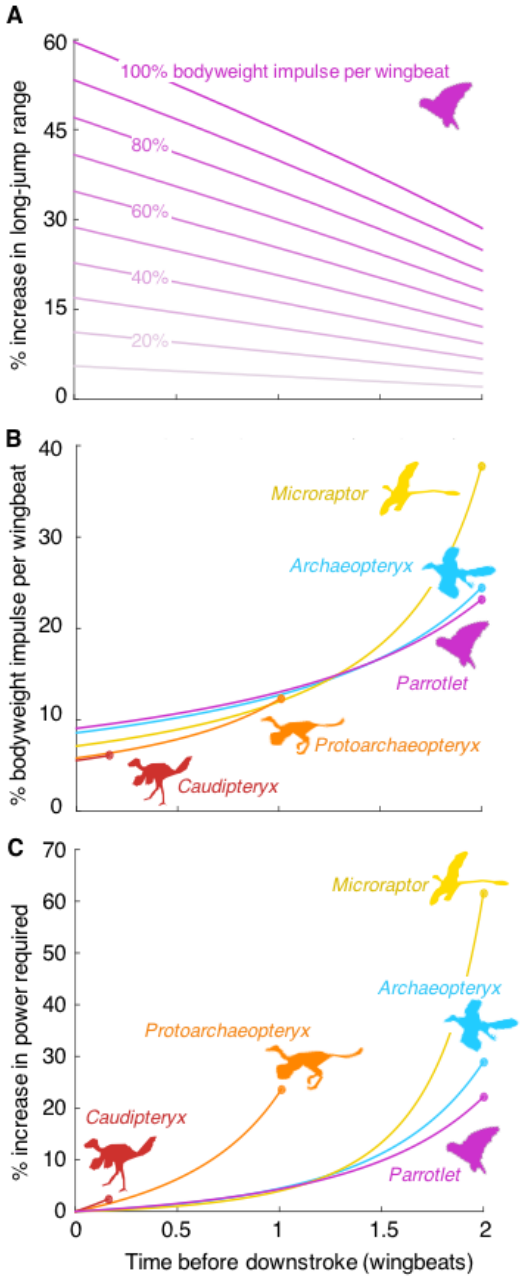

fig. S5. Effect of proto-wingbeat timing on distance and power required for a long jump. (**A**) Increasing the time between toe-off and the start of the downstroke decreases the long-jump range added by a parrotlet proto-wingbeat. The penalty from sub-optimal wingbeat timing is more significant for wingbeats that provide more weight support. (**B**) Delaying the downstroke increases the proto-wingbeat impulse required for parrotlets and bird antecedents to increase their long-jump range by 5%. These delayed proto-wingbeats were limited to those that require a muscle mass-specific power within what parrotlets require for a downstroke with full weight

support. (**C**) The higher wingbeat impulse needed to achieve the 5% range increase when a wingbeat is delayed, shown in (B), requires more aerodynamic power. We show here the percent increase relative to a wingbeat made immediately after toe-off (zero time delay).

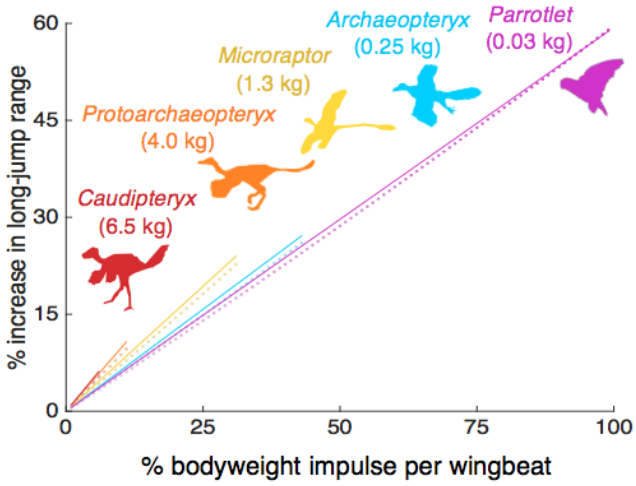

fig. S6. Linear approximation for the long-jump range versus wingbeat impulse. The linearized equation for the bimodal model $\Delta X \approx \frac{2gt_{DS}}{v_{TO,z}} J_{WB}$) closely approximates the relation between long-jump range and downstroke weight support. Solid lines show analytical results from applying the equation, dotted lines show results from the simulation (Fig. 4B).

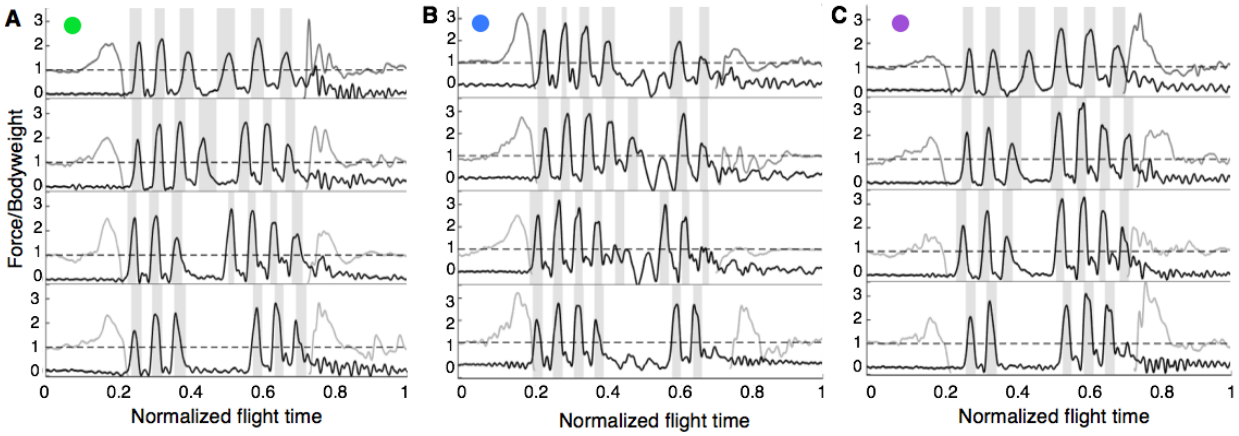

fig. S7. Representative force traces of individuals during 75-cm flights. Wingbeat patterns differed among the four parrotlets, as shown by representative flights from all four birds listed from top to bottom, for (**A**) level 75 cm flights, (**B**) ascending 75 cm flights, and (**C**) descending 75 cm flights. Flights by the same individual are shown in the same row of each panel. Each flight shows the bird's most commonly selected wingbeat pattern for each flight variation (see *Analyzed wingbeats from 75 cm flights*). Colored circles encode flight variations, as in the main text figures. Gray lines indicate vertical leg force, black lines indicate vertical wing force.

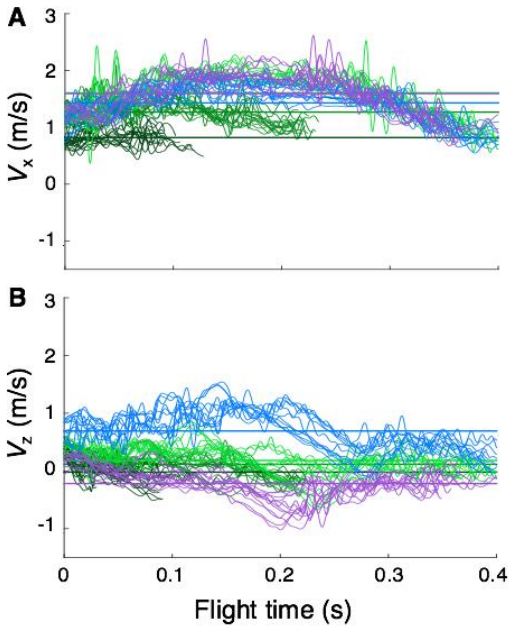

fig. S8. Velocity components during flight. Birds accelerated to average flight velocities within the first wingbeat, and braked mostly horizontally for landing. Velocity of the bird in the (**A**) horizontal direction and (**B**) vertical direction from toe-off to touch-down. Plots show velocity components (low-pass filtered, 100 Hz cutoff) for individual flights from each variation: 20 cm level ($\gamma = 0^o$; dark green), 40 cm level (green), 75 cm level (light green), 75 cm ascending ($\gamma = +20^o$; light blue), and 75 cm descending ($\gamma = -20^o$; purple). Horizontal lines show the time-average of all flights within each variation (*N*=4; *n*=5 for 20 and 40 cm flights, *n*=3 for 75 cm flights).

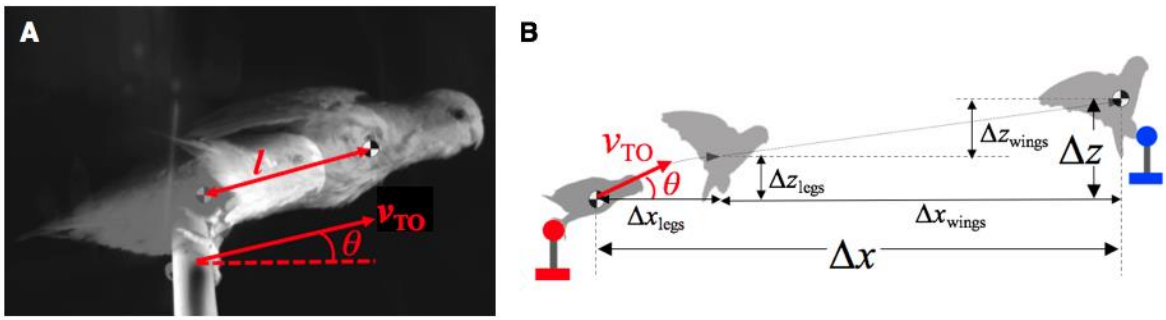

fig. S9. Key parameters used in modeling bird foraging flights. (**A**) Images of a parrotlet at the start and end of takeoff, illustrating the takeoff angle θ, takeoff velocity v_{TO}, and pushoff range *l*. (**B**) The horizontal and vertical displacements from the legs (Δx_{legs}, Δz_{legs}) and the wings (Δx_{wings}, Δz_{wings}) sum up to the total displacements from the end of takeoff (toe-off) to the start of landing (touch-down) (Δx, Δz).

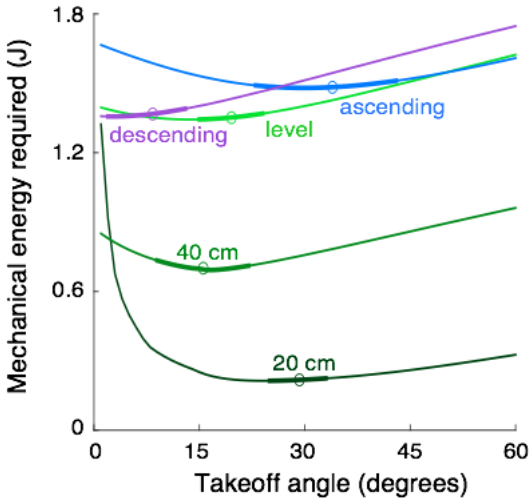

fig. S10. Mechanical energy model results assuming zero elastic storage. Our model predicts that parrotlets consistently select energy-minimizing takeoff angles, regardless of whether we assume inertial power is entirely elastically stored or dissipated. The principal effect of assuming zero elastic storage is an upwards shift in the required mechanical energy compared to full elastic storage (Fig. 4A).

Supplementary Tables

table S1. Takeoff and landing velocity data from Fig. 3 (A and B). Results shown are averages and standard deviations for *N*=4 birds, *n*=5 flights per bird for 20 and 40 cm variations and *n*=3 flights per bird for 75 cm variations (see *Instrumented Perches* and *Analyzed wingbeats from 75 cm flights* for flight selection explanations). The takeoff angle values shown in parentheses were calculated based on the vertical and horizontal impulse measured by the force sensors (*N*=4, *n*=5). All other values are determined from tracking the bird's eye in the high-speed videos.

Flight Variation	Level 20 cm	Level 40 cm	Level 75 cm	Ascending 75 cm	Descending 75 cm
Takeoff Angle	$29.2^o \pm 3.9^o$ ($19.3^o \pm 10.4^o$)	$15.5^o \pm 6.5^o$ ($11.9^o \pm 4.4^o$)	$19.5^o \pm 4.5^o$ ($9.8^o \pm 4.8^o$)	$33.9^o \pm 10.0^o$ ($29.9^o \pm 5.9^o$)	$8.3^o \pm 5.5^o$ ($1.5^o \pm 5.2^o$)
Landing Angle	$14.0^o \pm 9.1^o$	$8.3^o \pm 6.8^o$	$6.0^o \pm 6.6^o$	$-13.3^o \pm 10.2$	$11.1^o \pm 9.8^o$
Takeoff Speed (m/s)	1.05 ± 0.15	1.32 ± 0.11	1.33 ± 0.11	1.33 ± 0.07	1.30 ± 0.08
Landing Speed (m/s)	0.86 ± 0.16	1.02 ± 0.12	0.98 ± 0.17	0.90 ± 0.17	1.03 ± 0.23

table S2. Mechanical energy model input parameter values and predictions for foraging flight. The input parameters (shaded blue) were used to obtain the predictions (shaded gray) shown in Fig. 4A (average takeoff angles θ from table S1 are repeated here for comparison). Minimum energy estimates calculated assuming zero elastic storage are shown in parentheses. Note that horizontal and vertical displacements from toe-off to touch-down (Δx, Δz; fig. S9B) do not match the actual distances between the perches themselves due to leg extension (fig. S9A) and body orientation.

Flight Variation	**Level 20 cm**	**Level 40 cm**	**Level 75 cm**	**Ascending 75 cm**	**Descending 75 cm**
Δx (cm)	9	27	60	57	57
Δz (cm)	0	2	6	28	-8
V_{avg} (m/s)	0.85	1.3	1.6	1.6	1.6
Average θ	29.2° ± 3.9°	15.5° ± 6.5°	19.5° ± 4.5°	33.9° ± 10.0°	8.3° ± 5.5°
Predicted energy-minimizing θ	24.2	16.4	13.7°	30.0°	2.6°
Standard deviations between predicted and average θ	-1.3	+0.1	-1.3	-0.4	-1.0
Minimum energy	0.21 J (0.21 J)	0.41 J (0.69 J)	0.75 J (1.34 J)	0.77 J (1.48 J)	0.74 J (1.36 J)
Locomotion time	0.09 s	0.21 s	0.38 s	0.40 s	0.36 s

table S3. Time rate of change of the tau function ($\dot{\tau}$). These $\dot{\tau}$ values correspond to slopes of linear regressions for the tau function; corresponding R^2 values for the linear regressions indicate that $\dot{\tau}$ was held constant prior to landing. Values of $\dot{\tau}$ between 0.5 and 1 indicate that the parrotlet landings were "controlled collisions". Averages and standard deviations are given for N=4 birds, n=5 flights each for 20 and 40 cm variations and n=3 flights each for 75 cm variations.

Flight Variation	**Level 20 cm**	**Level 40 cm**	**Level 75 cm**	**Ascending 75 cm**	**Descending 75 cm**
$\dot{\tau}$	1.12 ± 0.15	0.84 ± 0.07	0.76 ± 0.04	0.74 ± 0.07	0.77 ± 0.03
R^2	0.95 ± 0.04	0.96 ± 0.02	0.97 ± 0.01	0.98 ± 0.004	0.98 ± 0.01

table S4. Bird antecedent parameters from Dececchi *et al*. (*35*) used in the protowing model. Values for hindlimb length and estimated no-flap takeoff speed are from supplementary table S10 in (*36*). Values for mass, wing length, wing area and flapping frequency are from supplementary table S18 in (*36*). Flight muscle mass was estimated as 10% of bodymass (see Materials and Methods).

Dinosaur	**Mass (kg)**	**Hindlimb length (m)**	**Wing length (m)**	**Total wing area (m^2)**	**Flapping frequency (Hz)**	**Estimated no-flap takeoff speed at 30°**
Archaeopteryx	0.25	0.16	0.26	0.0479	11.3	2.26
Microraptor	1.25	0.29	0.49	0.1410	7.8	2.74
Protoarchaeopteryx	4.0	0.37	0.28	0.0178	5.9	2.94
Caudipteryx	6.5	0.47	0.20	0.0276	5.3	3.17